Matter, Volume *8*

Supplemental information

Pyrolyzed preceramic precursors to compositionally complex ceramics

Saurabh Khuje, Jiayue Sun, Chong Yang, Zhongxuan Wang, Long Zhu, Tangyuan Li, Gianna Valentino, Nicholas Ku, Andres Bujanda, Jian Yu, Tucker Moore, Taylor J. Woehl, Liangbing Hu, and Shenqiang Ren

SUPPLEMENTAL INFORMATION

Pyrolyzed Preceramic Precursors to Compositionally Complex Ceramics

Saurabh Khuje,[1] Jiayue Sun,[2] Chong Yang,[3] Zhongxuan Wang,[1] Long Zhu,[1] Tangyuan Li,[3] Gianna Valentino,[1] Nicholas Ku,[5] Andres Bujanda,[5] Jian Yu,[5] Tucker Moore,[5] Taylor J. Woehl,[2] Liangbing Hu,[3,4,*] Shenqiang Ren[1,*]

[1]Department of Materials Science and Engineering, University of Maryland, College Park, MD, 20742, US
[2]Department of Chemical and Biomolecular Engineering, University of Maryland, College Park, MD, 20742, US
[3]Department of Electrical and Computer Engineering, Yale University, New Haven, CT, 06511, US
[4]Center for Materials Innovation, Yale University, New Haven, CT, 06511, US
[5]DEVCOM Army Research Laboratory, Aberdeen Proving Ground, MD, 21005, US
*Correspondence: liangbing.hu@yale.edu, sren@umd.edu

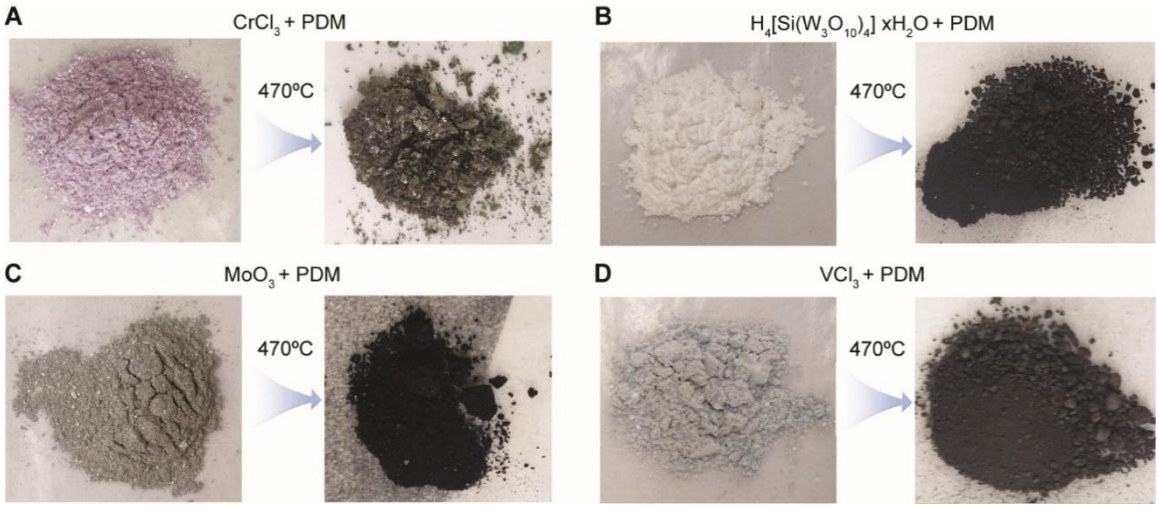

Figure S1. Optical images for multi-element ceramic powders after thermal curing for crosslinking purposes.
(A) Chromium (III) chloride as the crosslinker.
(B) Tungstosilicic acid hydrate as the crosslinker.
(C) Molybdenum trioxide as the crosslinker.
(D) Vanadium (III) chloride as the crosslinked metal.

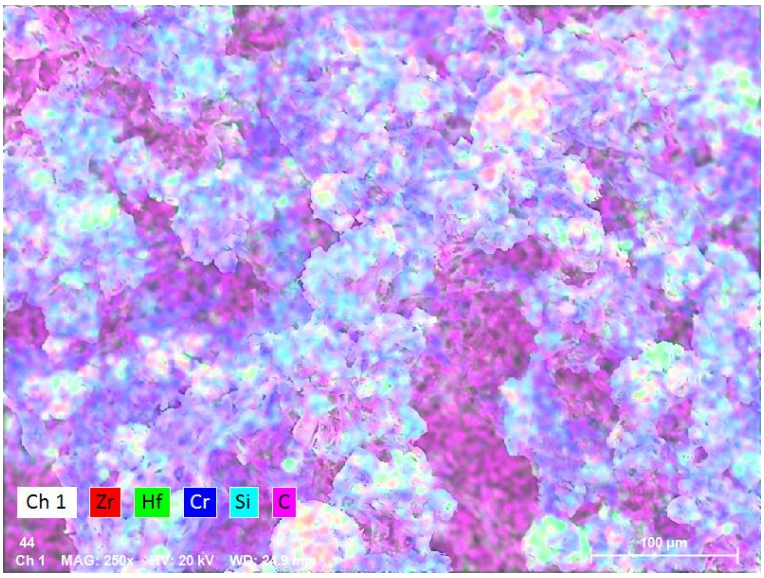

Figure S2. EDS mapping of preceramic precursor with multiple transition elements as the starting precursor.

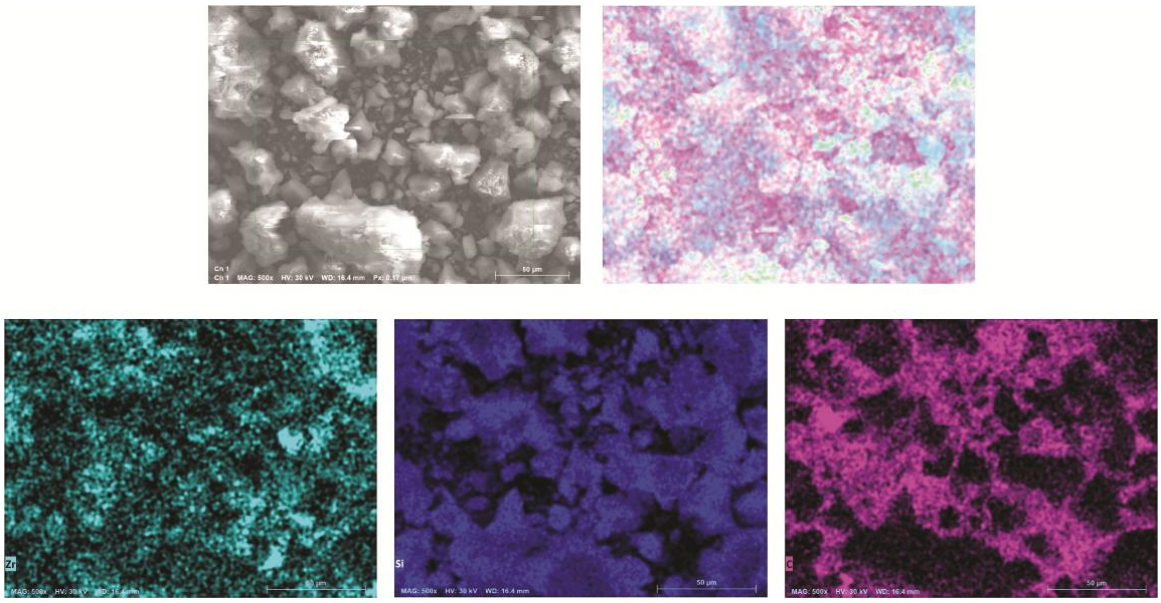

Figure S3. Lower magnification SEM and corresponding individual EDS maps for Zr-PCS preceramic powders following crosslinking.

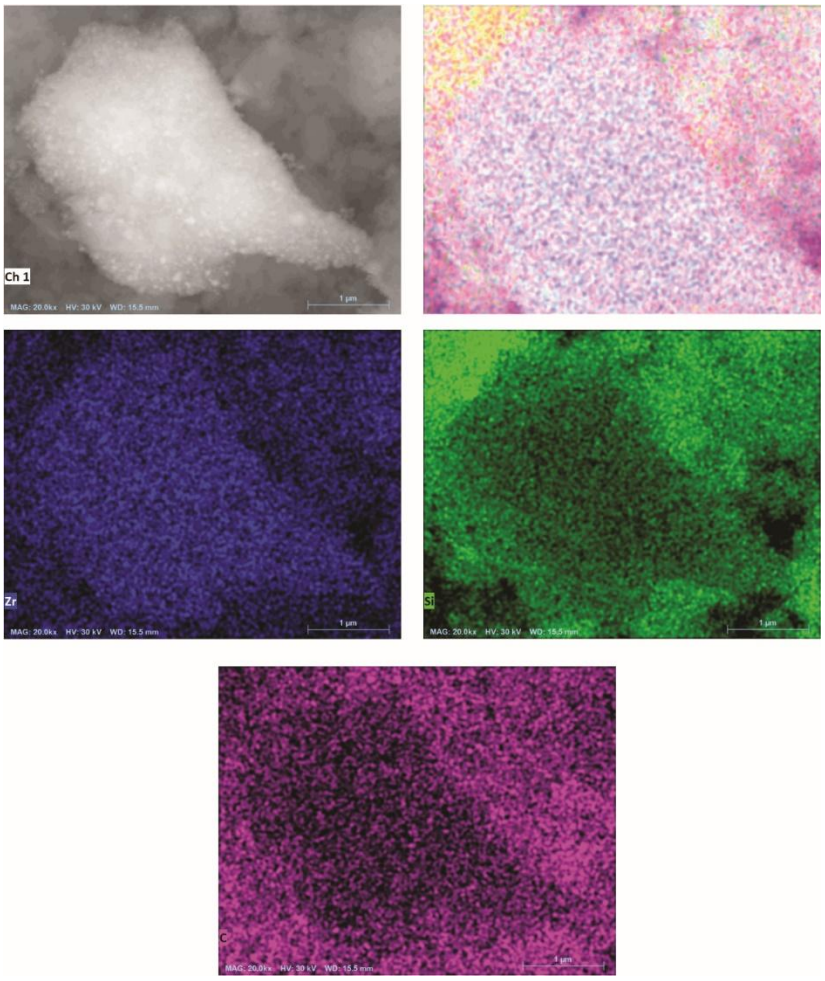

Figure S4. Magnified SEM and individual EDS maps for Zr-PCS preceramic powders following crosslinking.

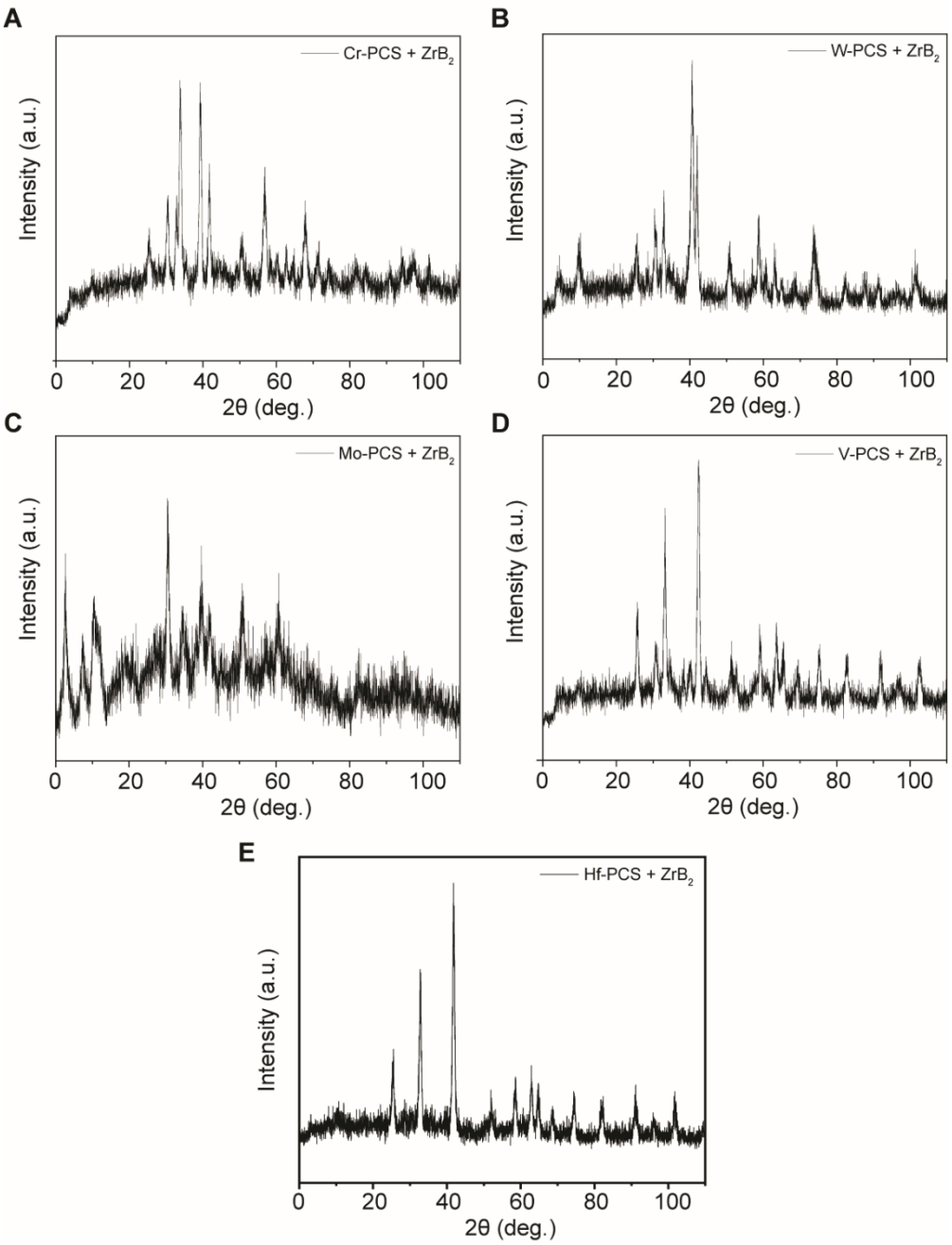

Figure S5. XRD plots for multi-element ceramic powders pyrolysed at elevated temperatures.
(A) Chromium (Cr) as the crosslinked metal with ZrB_2 filler.
(B) Tungsten (W) as the crosslinked metal with ZrB_2 filler.
(C) Molybdenum (Mo) as the crosslinked metal with ZrB_2 filler.
(D) Vanadium (V) as the crosslinked metal with ZrB_2 filler.
(E) Hafnium (Hf) as crosslinked metal with ZrB_2 filler.

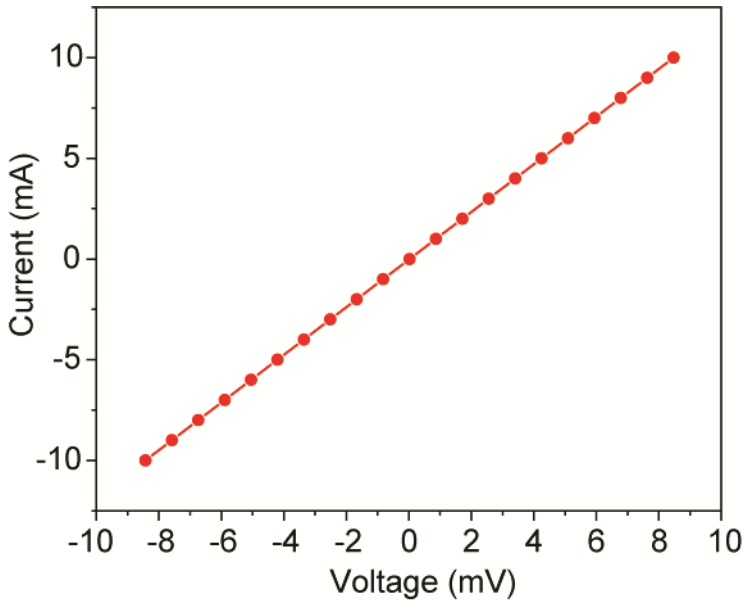

Figure S6. I-V characteristics of ZrB_2 sample prepared using ultra high temperature sintering.

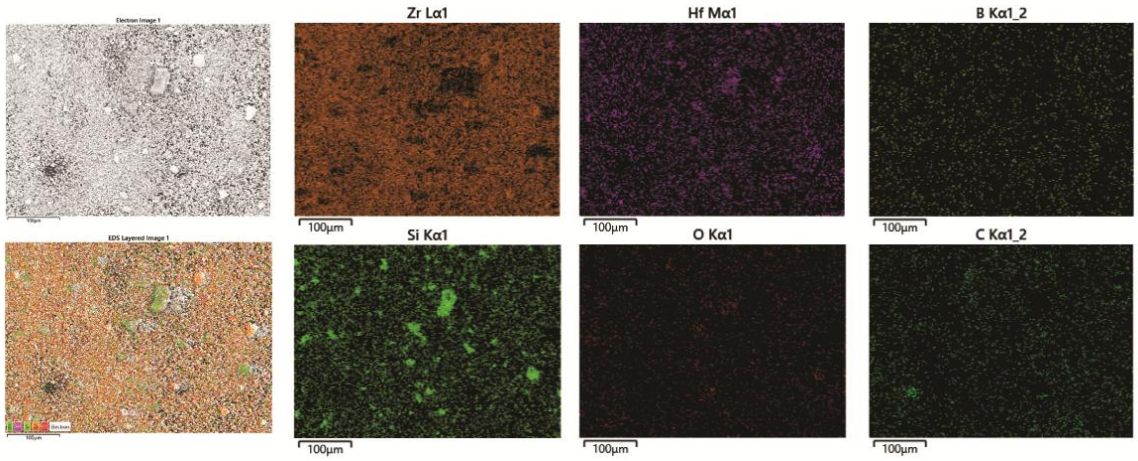

Figure S7. SEM and EDS mapping for plots for Hf-PCS preceramic powders pyrolyzed at elevated temperatures with ZrB_2 filler particles.

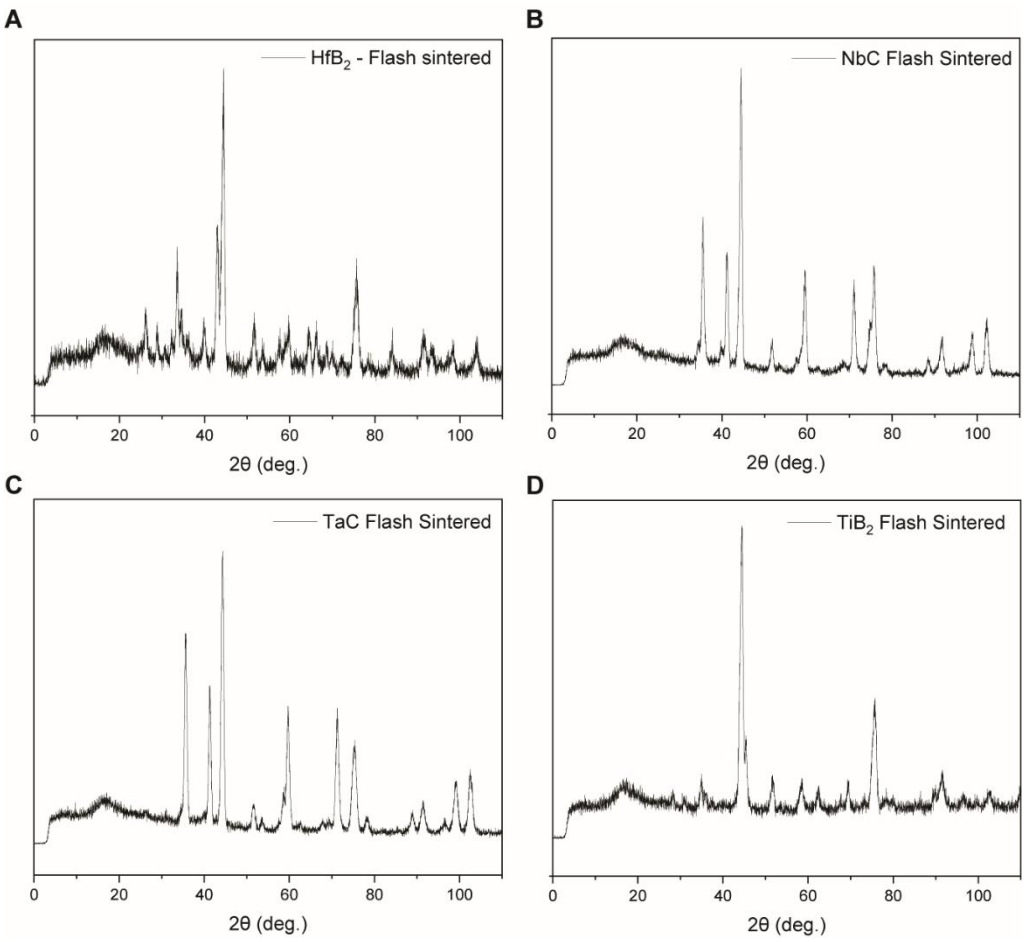

Figure S8. XRD plots for Zr-PCS preceramic powders pyrolysed at elevated temperatures with different fillers.

(A) With HfB_2 as a filler.
(B) With NbC as a filler.
(C) With TaC as a filler.
(D) With TiB_2 as a filler.

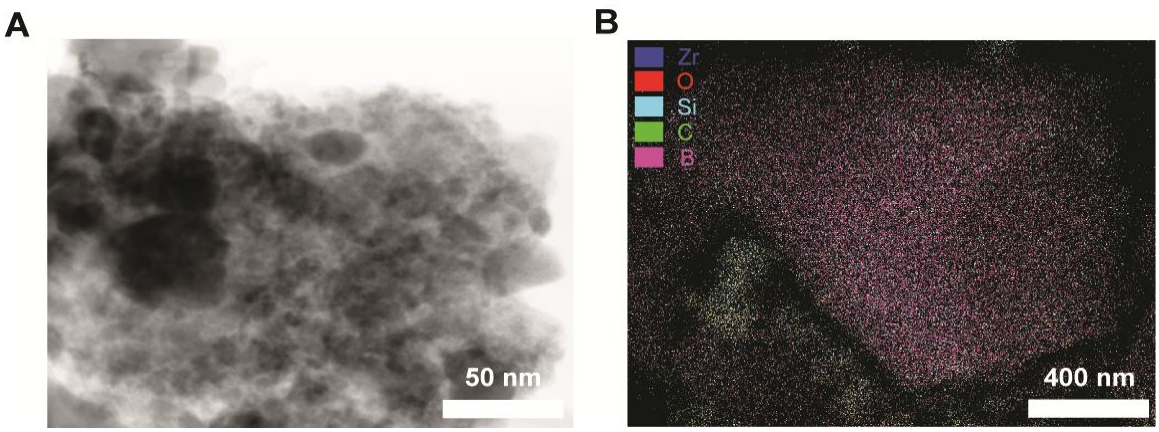

Figure S9. Additional microscopic images.
(A) TEM observation of Zr-Si-O-C-B particles.
(B) TEM-EDS mapping depicting element distribution.

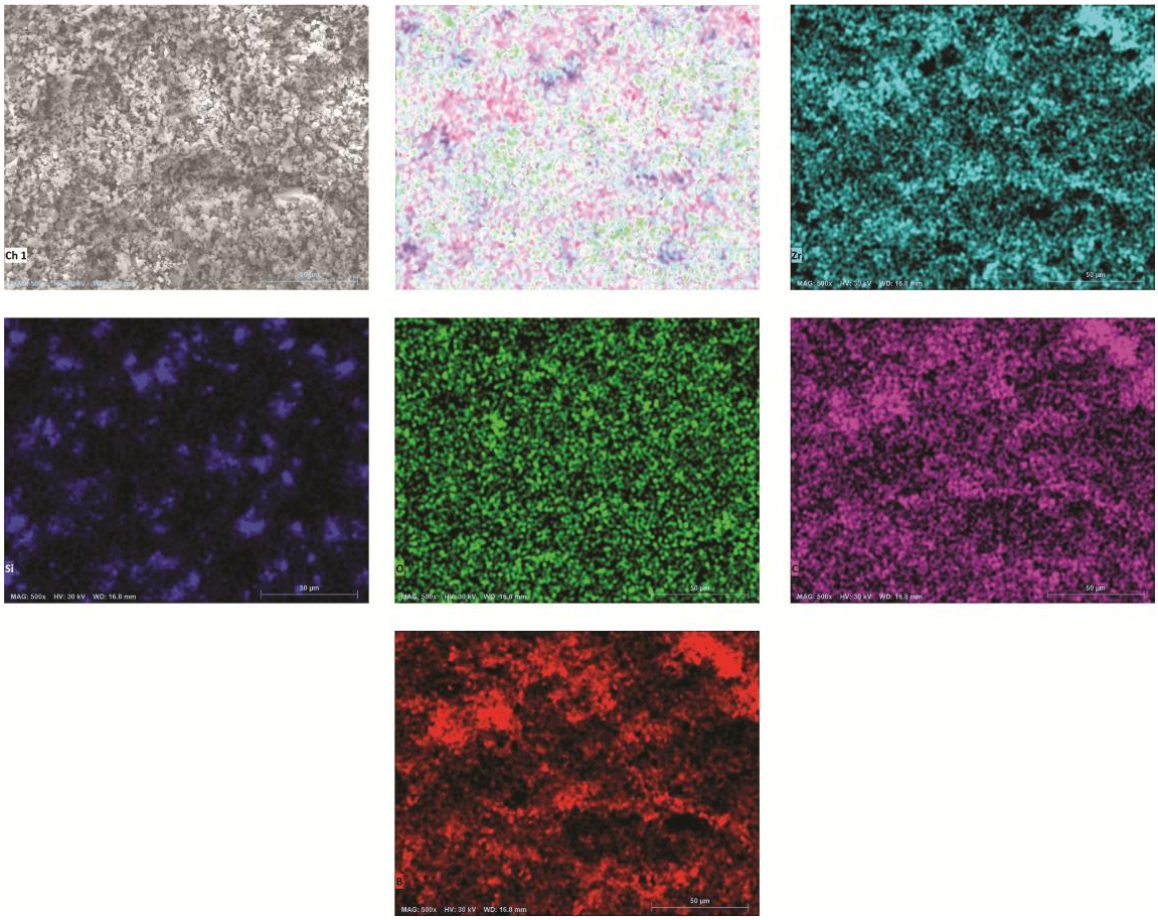

Figure S10. Low magnification SEM and individual EDS maps for Zr-Si-O-C-B preceramic precursor following pyrolysis at elevated temperatures.

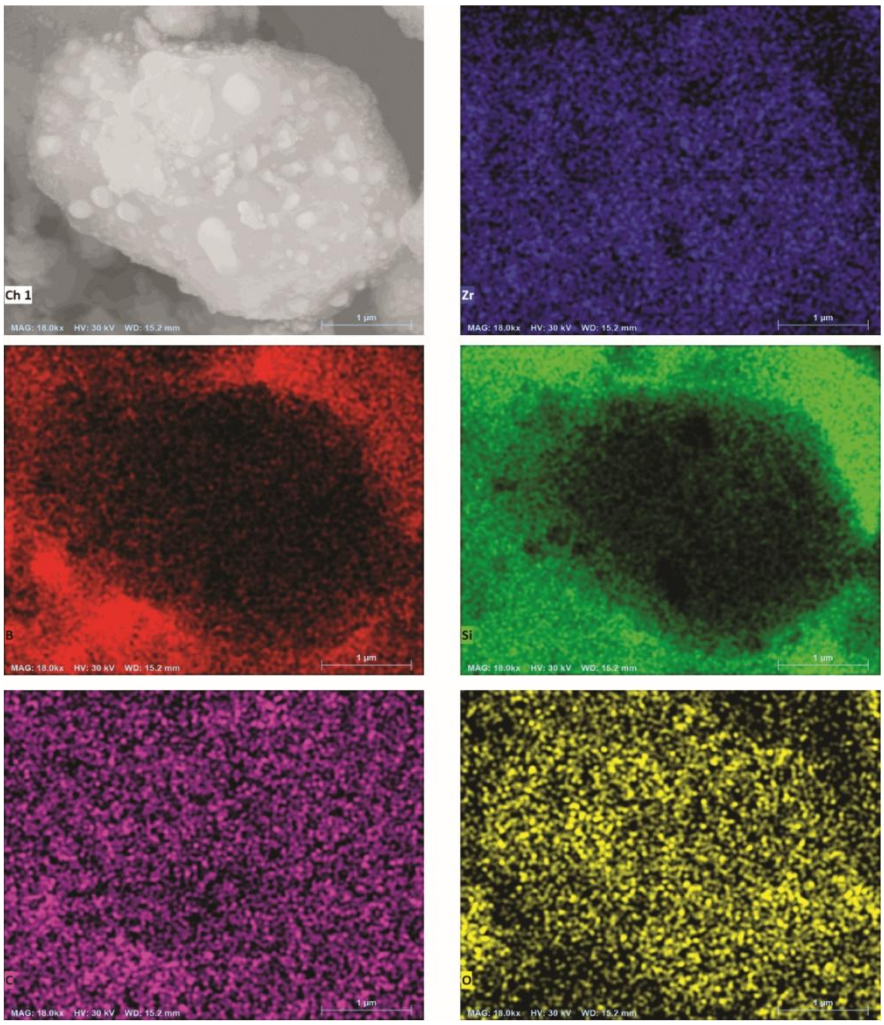

Figure S11. Magnified view of the SEM and individual EDS maps for Zr-Si-O-C-B preceramic precursor following pyrolysis at elevated temperatures.

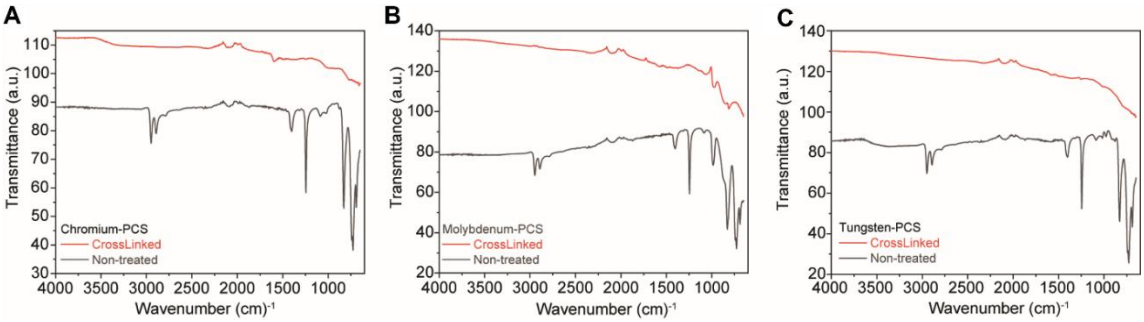

Figure S12. FTIR for pure additional transition metals following crosslinking reaction with PCS facilitated by thermal curing.

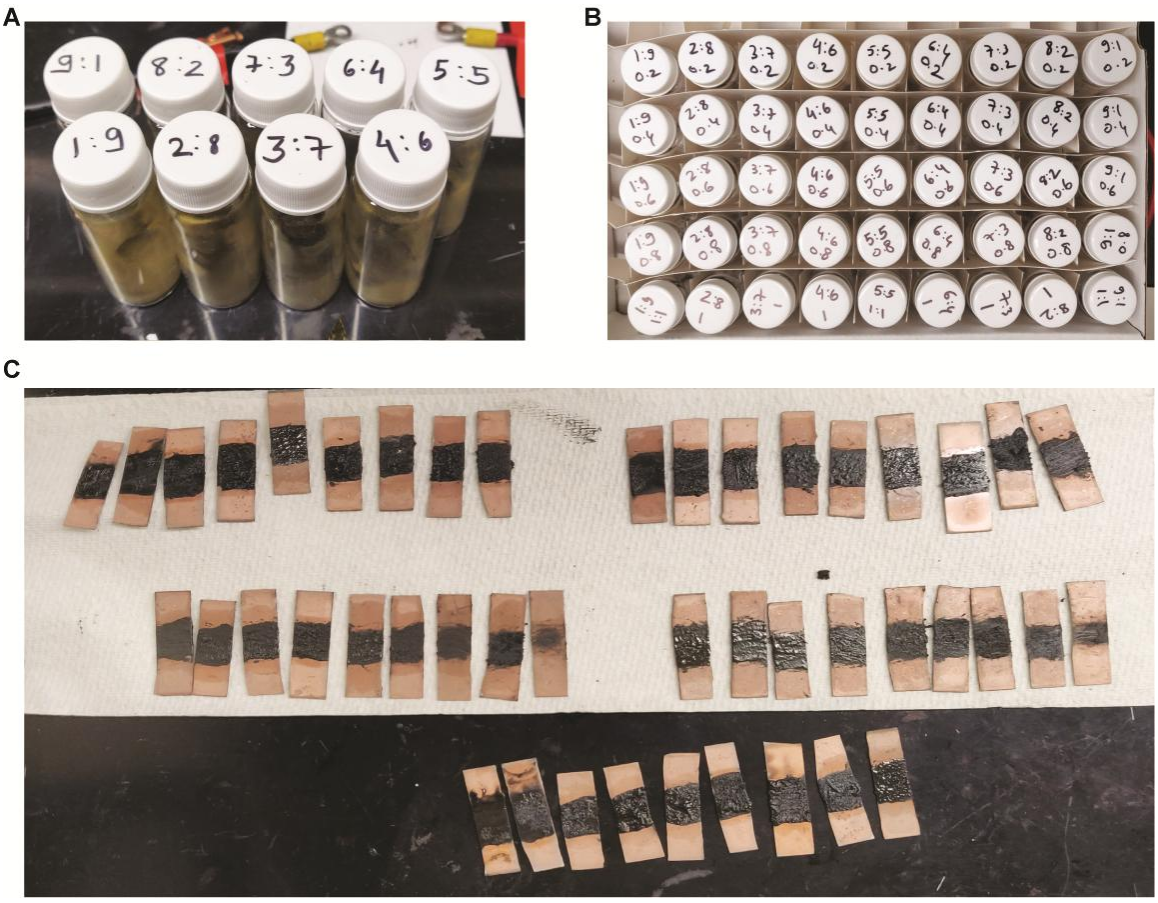

Figure S13. Samples prepared for high throughput analysis for determining the optimal precursor powder to solvent ratio.

(A) Samples with varying ratios of Zr-PCS to ZrB_2 powders.

(B) Batching for different ratios of preceramic powders and solvent ratios.

(C) Samples prepared via electrical pyrolysis for oxygen-hydrogen torch testing.

Table S1. Screening results for varying powder and solvent ratios.

ZrB_2 : Zr-PCS Ratio	ΔR for 1:0.2	ΔR for 1:0.4	ΔR for 1:0.6	ΔR for 1:0.8	ΔR for 1:1
1:9	--	19000	27564	37900	61370
2:8	--	21380	18390	52765	27308
3:7	3540	27009	33670	13653	17550
4:6	--	308.76	407.5	191	211
5:5	281.4	191.07	188.6	120.8	106.37
6:4	72.9	19.31	16.4	3.09	2.293
2:1	0.9802	0.4449	0.3344	0.427	0.666
7:3	1.55	1.03	0.285	0.83	0.3846
8:2	1.1	0.65	0.316	1.082	0.634
9:1	0.9	0.987	0.53	0.88	0.4736

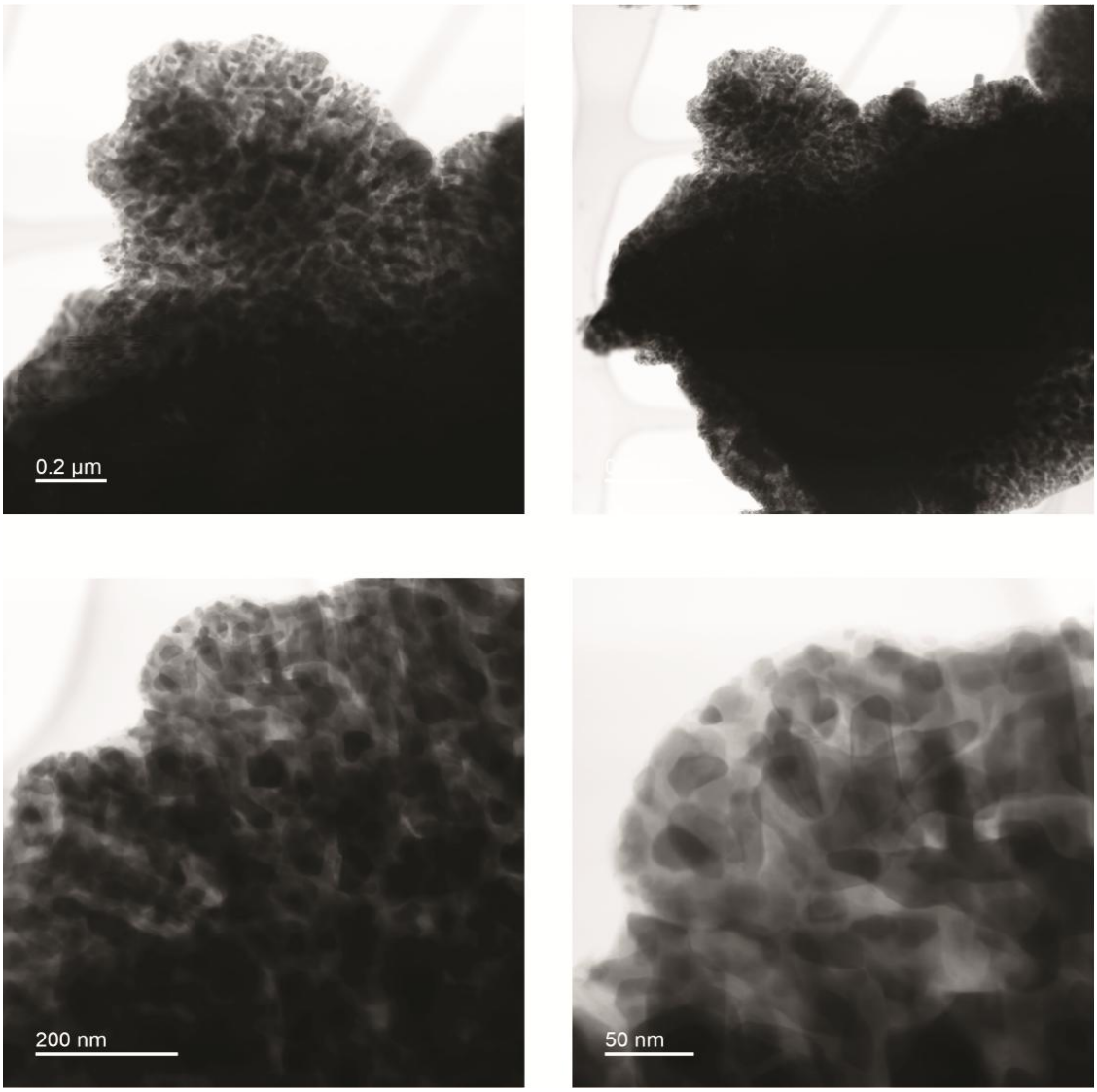

Figure S14. Low and high magnification TEM images for Zr-Si-O-C-B particles for particle size and distribution.

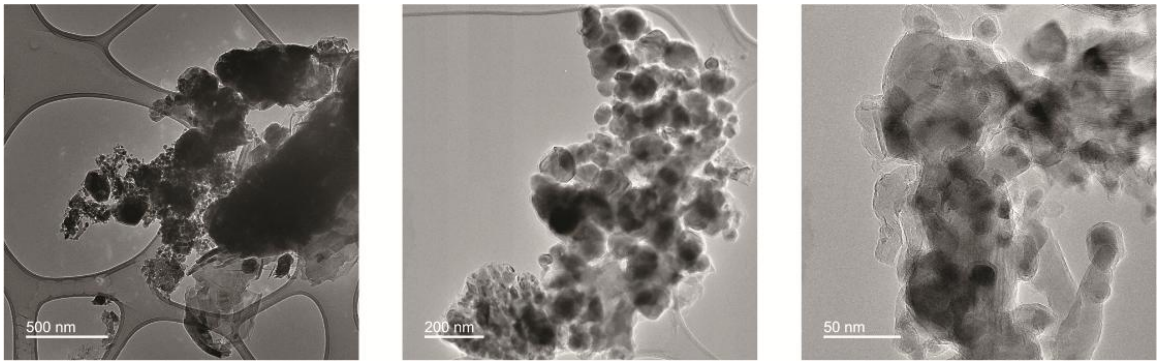

Figure S15. Additional low and high magnification TEM images for Zr-Si-O-C-B particles for different areas.

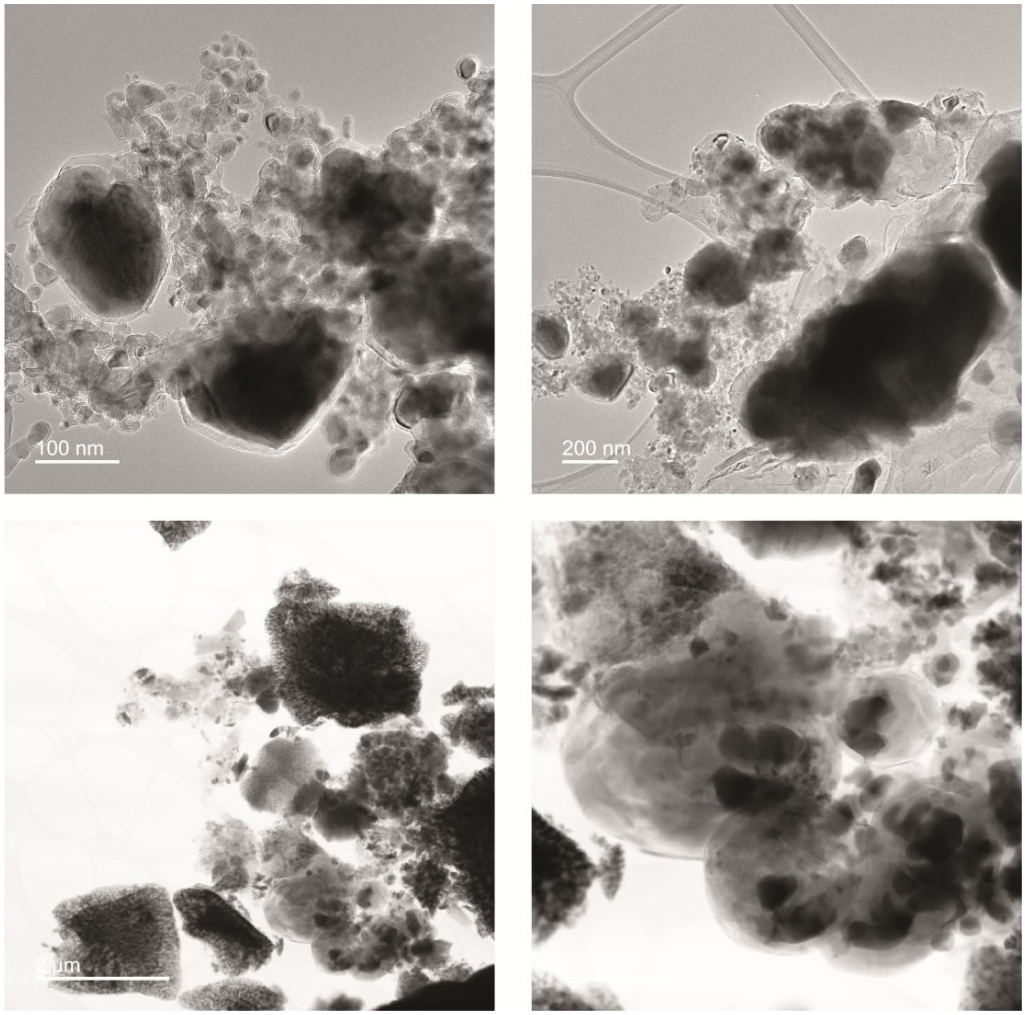

Figure S16. Additional low and high magnification TEM images for Zr-Si-O-C-B particles for different areas.

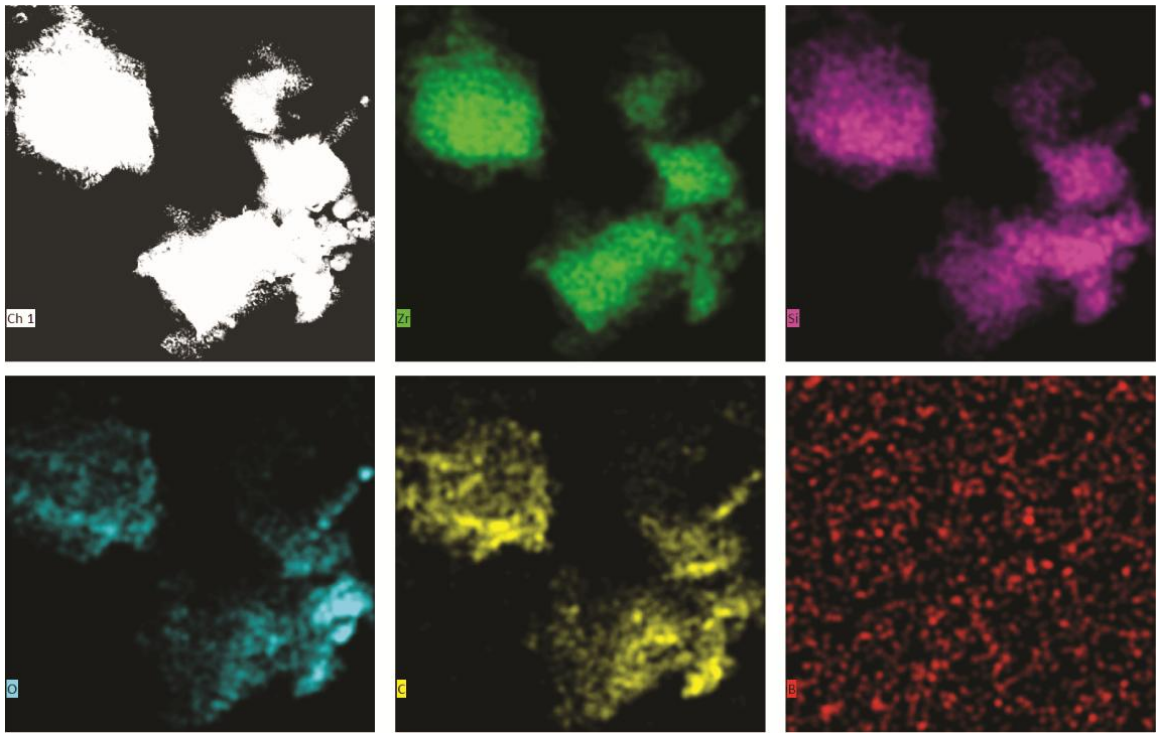

Figure S17. EDS analysis Zr-Si-O-C-B precursor for distribution of the individual elements Zr, Si, O, C and B (Area 1).

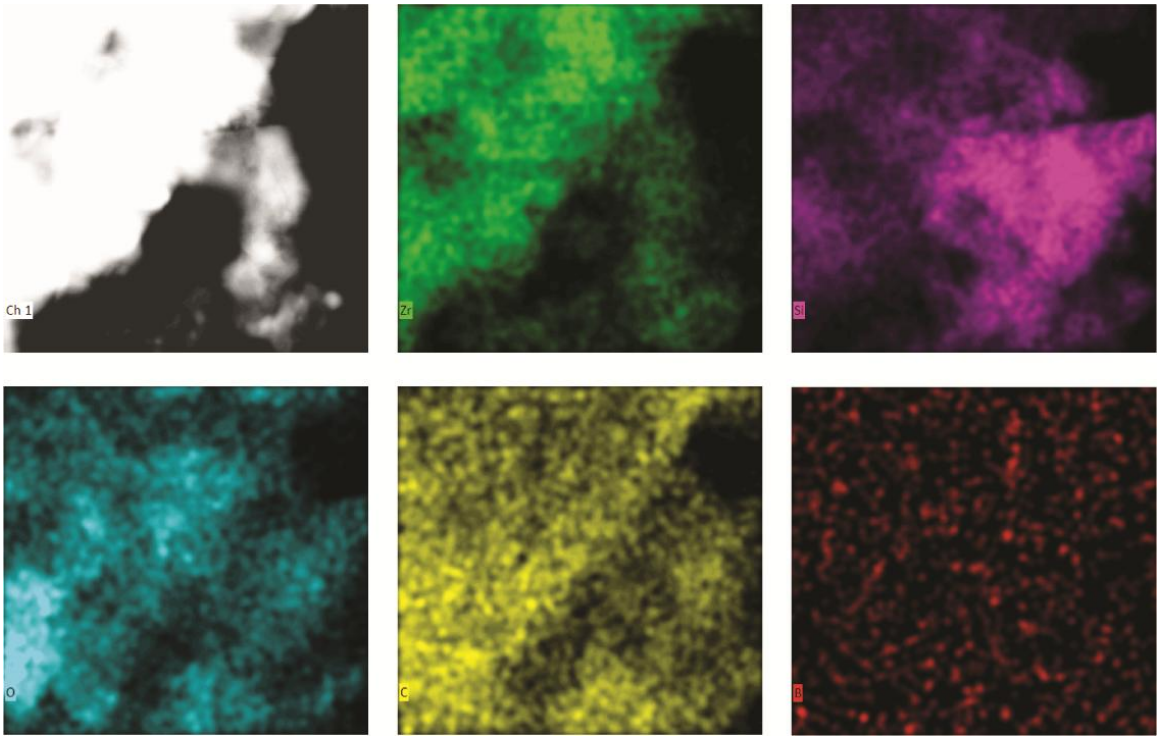

Figure S18. EDS analysis Zr-Si-O-C-B precursor for distribution of the individual elements Zr, Si, O, C and B (Area 2).

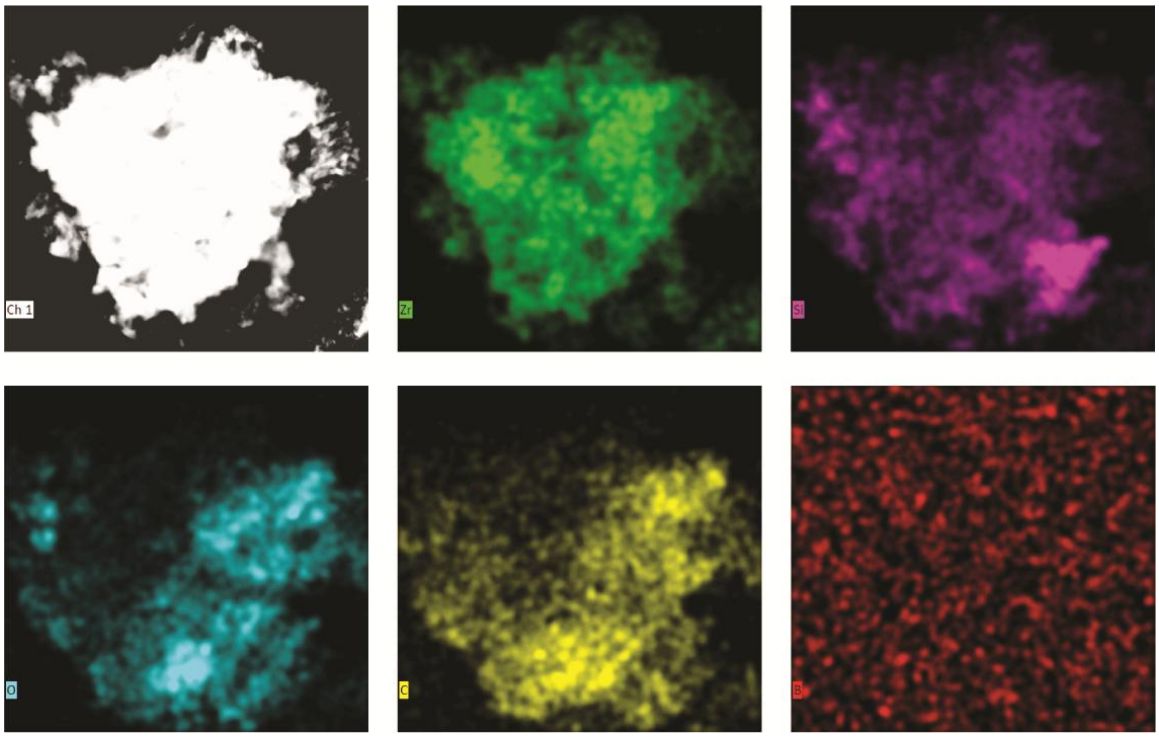

Figure S19. EDS analysis Zr-Si-O-C-B precursor for distribution of the individual elements Zr, Si, O, C and B (Area 3).

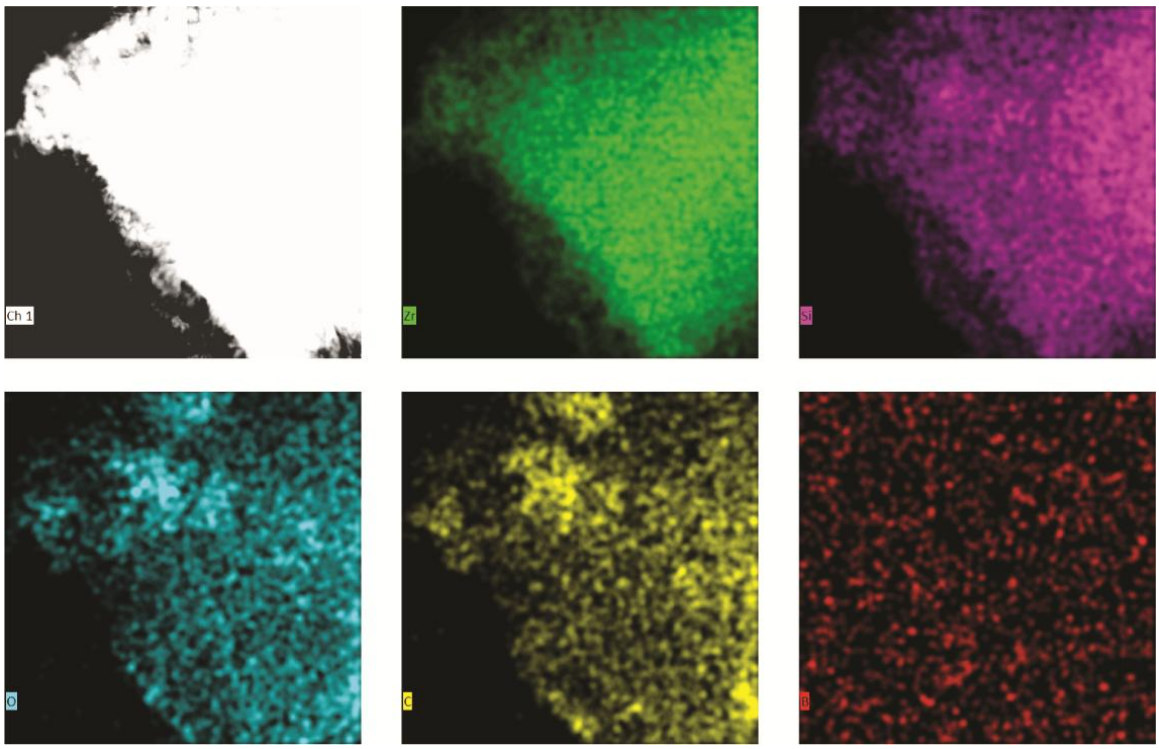

Figure S20. EDS analysis Zr-Si-O-C-B precursor for distribution of the individual elements Zr, Si, O, C and B (Area 4).

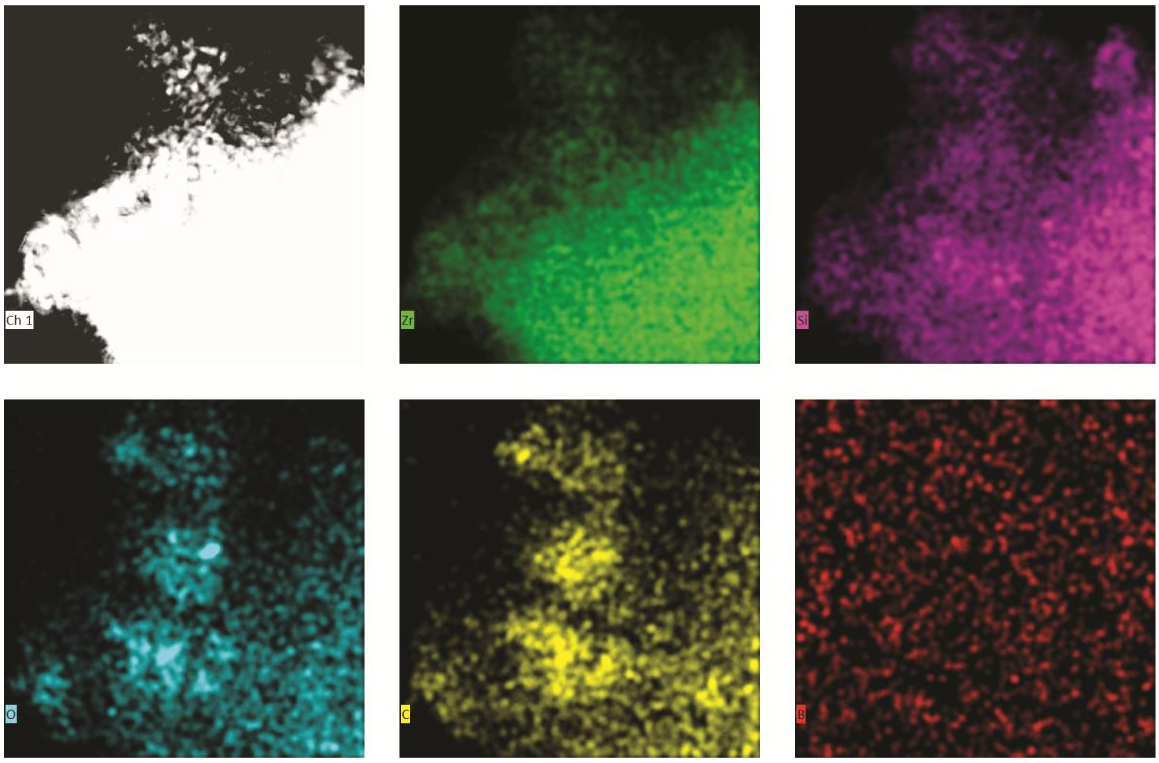

Figure S21. EDS analysis Zr-Si-O-C-B precursor for distribution of the individual elements Zr, Si, O, C and B (Area 5).

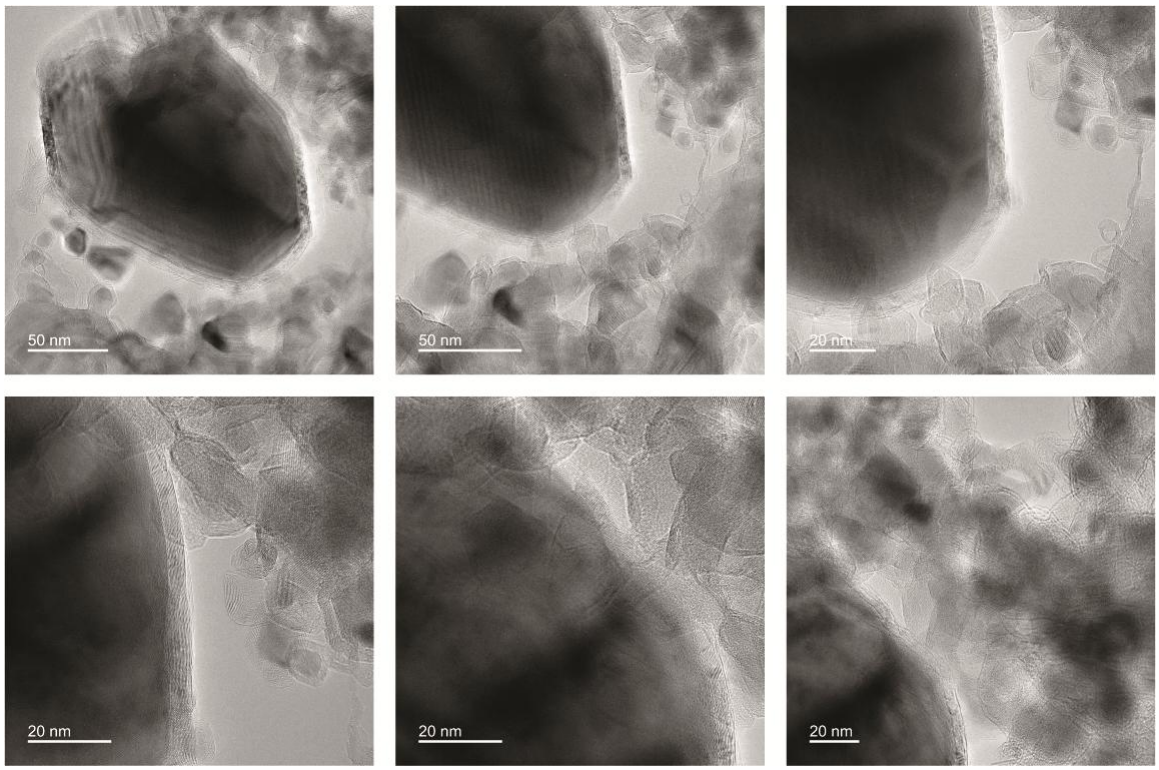

Figure S22. HR-TEM images demonstrate that the ZrB_2 particle is coated by an amorphous surface layer.

Figure S23. Optical image of the preceramic slurry deposited via extrusion-based processing onto a copper film prior to pyrolysis.

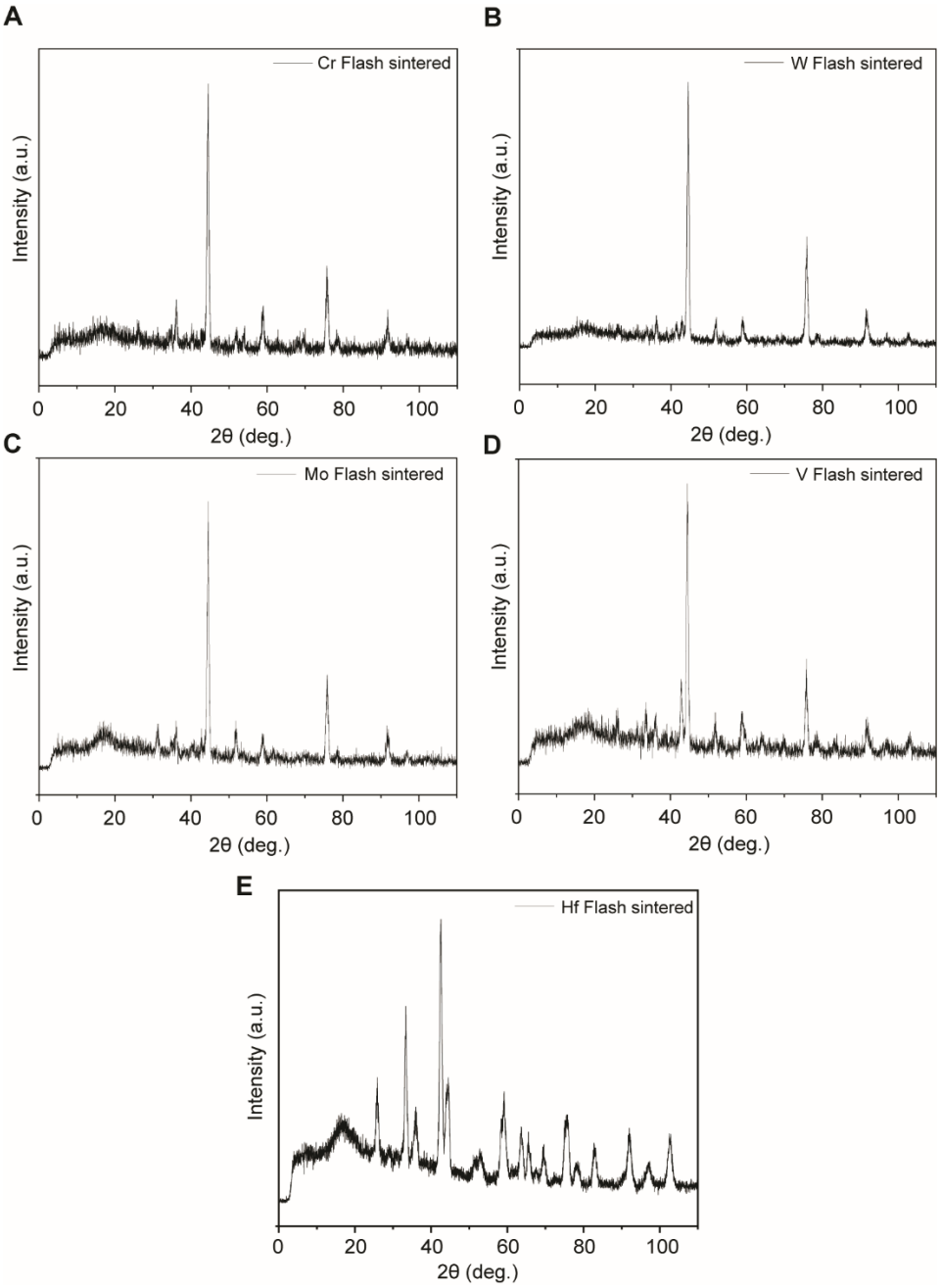

Figure S24. XRD plots for multi-element ceramic coatings after electrical pyrolysis.
(A) Cr as the crosslinked metal.
(B) W as the crosslinked metal.
(C) Mo as the crosslinked metal.
(D) V as the crosslinked metal.
(E) Hf as the crosslinked metal.

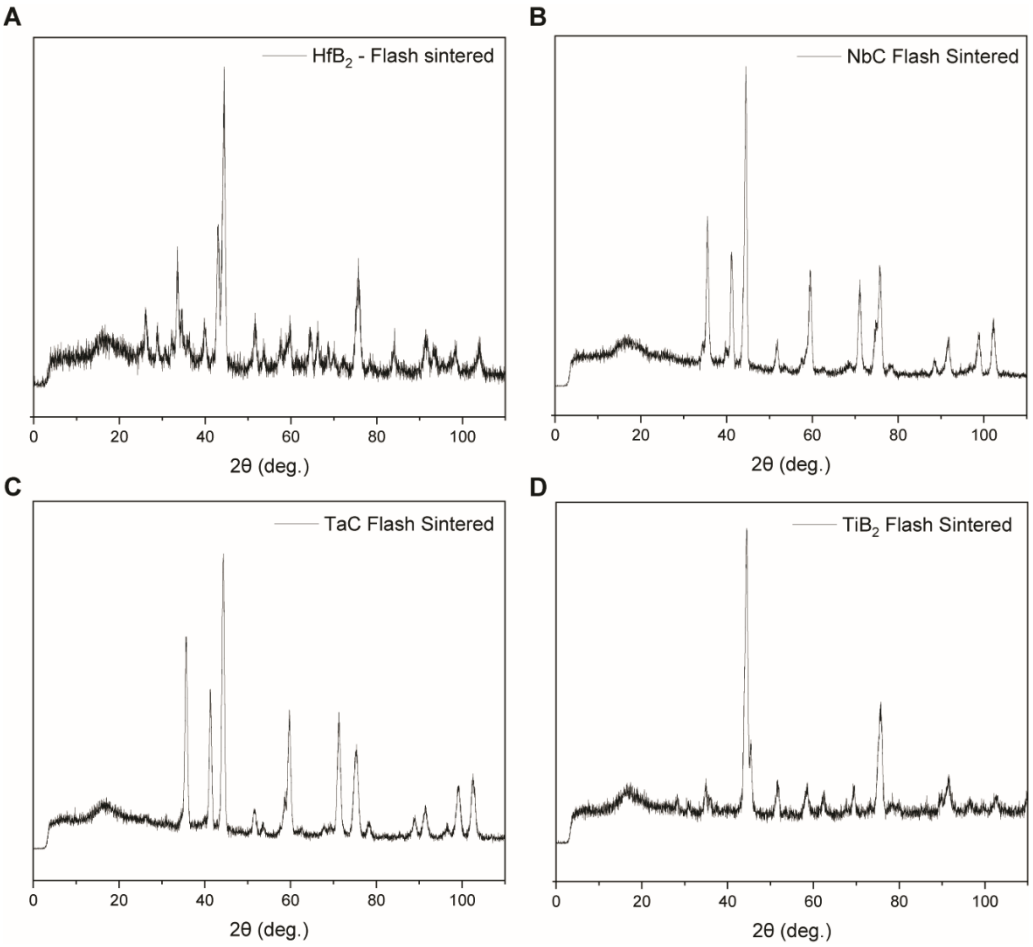

Figure S25. XRD plots for feedstock consisting of Zr-PCS powders with different fillers following electrical pyrolysis.

(A) With HfB_2 as a filler.
(B) With NbC as a filler.
(C) With TaC as a filler.
(D) With TiB_2 as a filler.

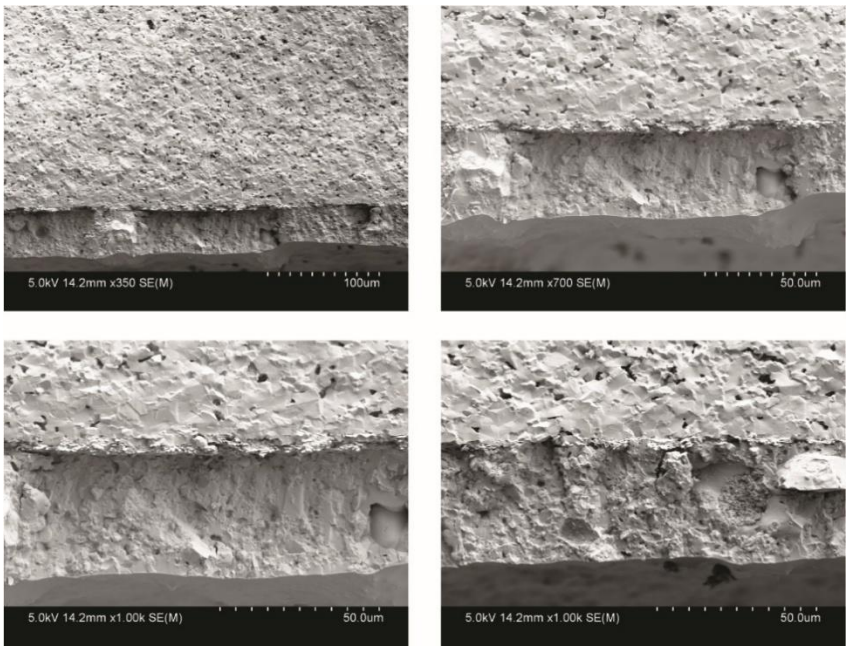

Figure S26. Additional SEM images depicting the cross-section of electrically pyrolyzed Zr-Si-O-C-B samples.

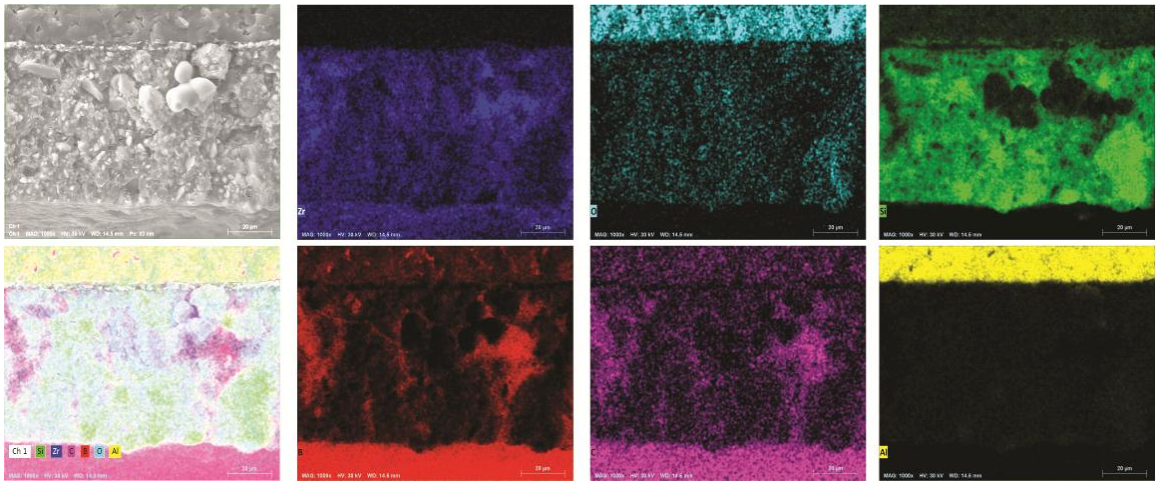

Figure S27. EDS mapping of the cross-section of electrically pyrolyzed Zr-Si-O-C-B sample.

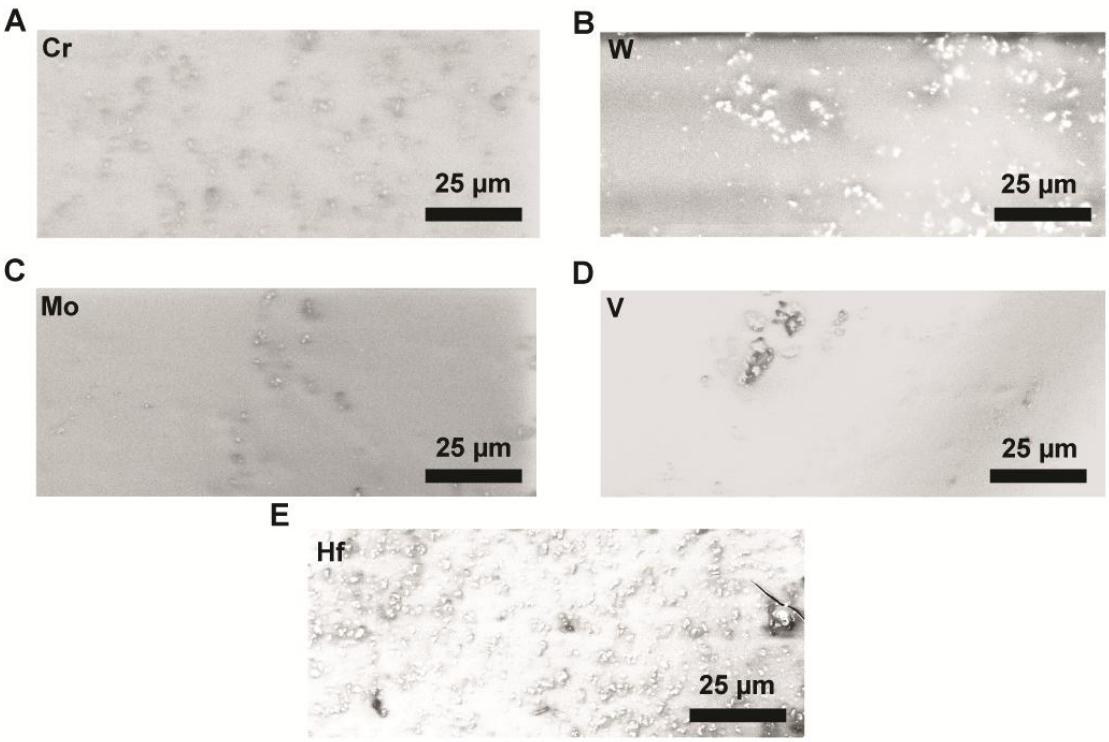

Figure S28. SEM observations for multi-element ceramic coatings after flash sintering.
(A) Cr as the crosslinked metal.
(B) W as the crosslinked metal.
(C) Mo as the crosslinked metal.
(D) V as the crosslinked metal.
(E) Hf as the crosslinked metal.

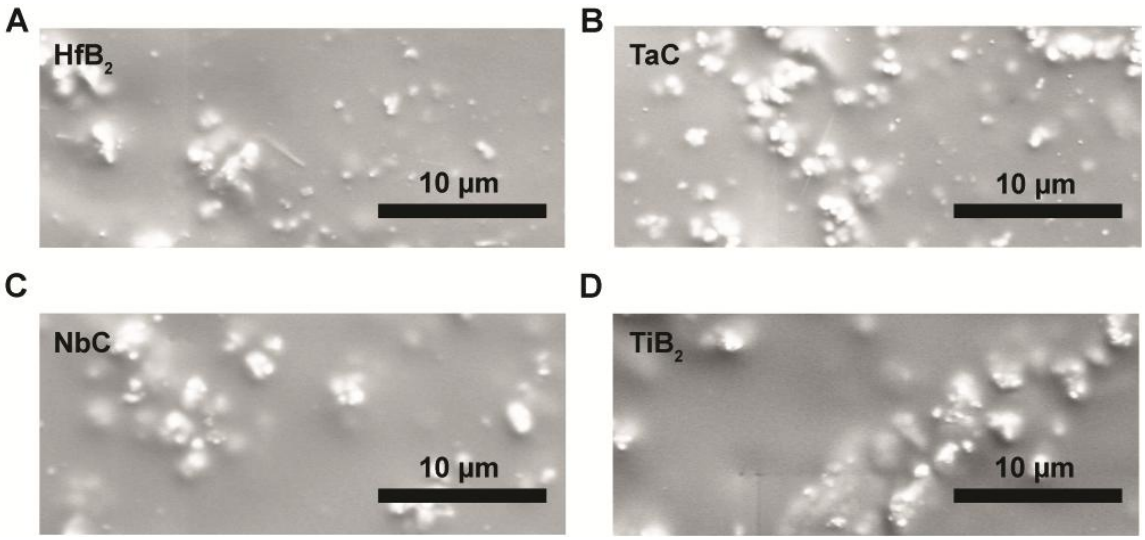

Figure S29. SEM observations for Zr-PCS powders with different fillers following flash sintering.
(A) With HfB_2 as a filler.
(B) With NbC as a filler.
(C) With TaC as a filler.
(D) With TiB_2 as a filler.

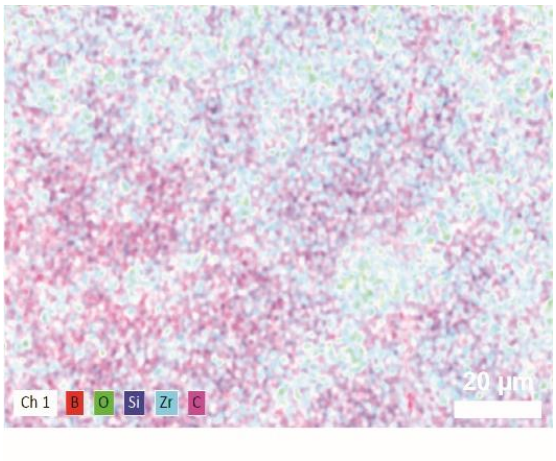

Figure S30. EDS mapping of Zr-Si-O-C-B (1:0.6) sample flash sintered at a power of 30W. The presence and uniform distribution of Zr, Si, O, C and B elements can be observed.

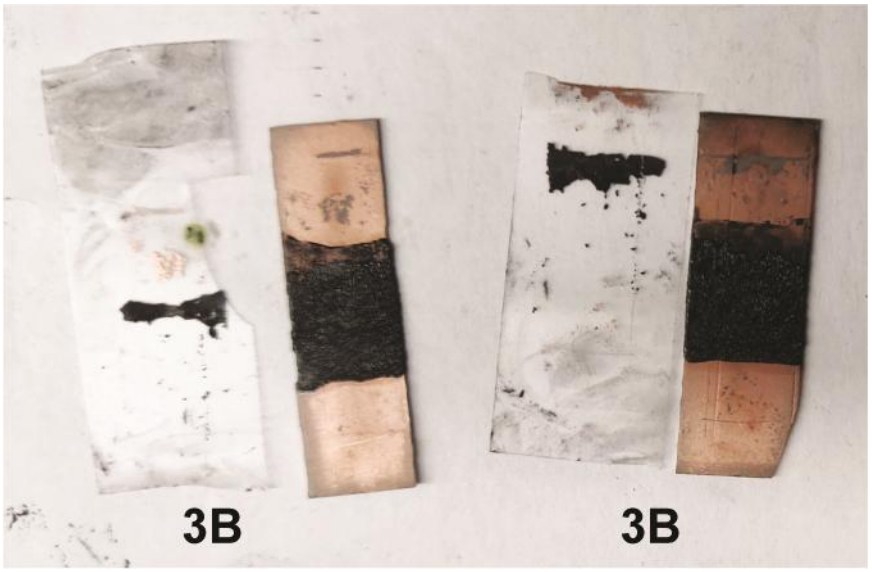

Figure S31. Adhesion testing of the electrically pyrolyzed Zr-Si-O-C-B sample, performed following ASTM D3359 crosshatch tape testing standards. The test reveals a 3B adhesion rating, corresponding to removal of 5–15% of the coating area, indicative of moderate adhesion typical for pyrolyzed ceramic coatings on metallic substrates without additional surface pretreatment.

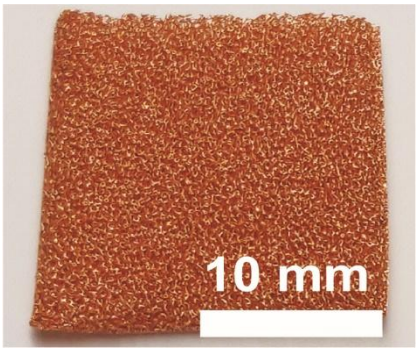

Figure S32. Copper foam prior to coating it with Zr-Si-O-C-B slurry.

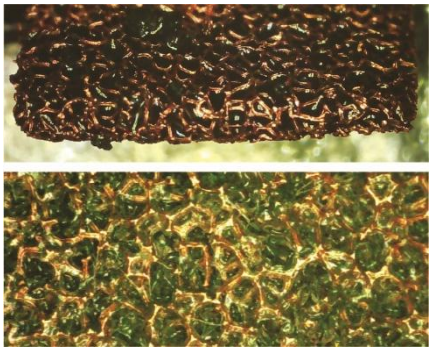

Figure S33. Plane and isometric images of coated foam as observed through an optical microscope.

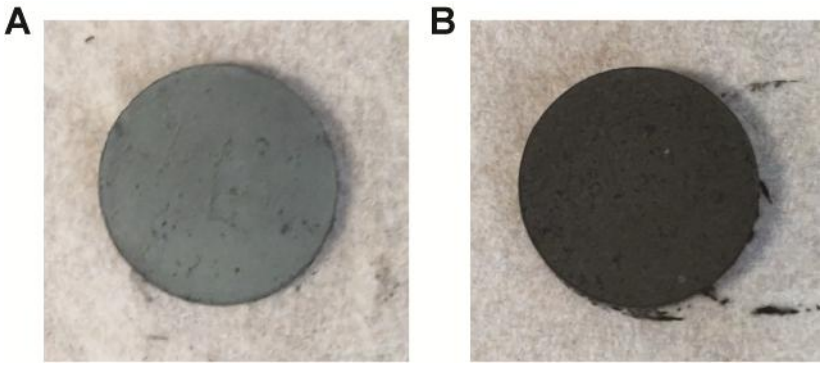

Figure S34. Optical image of the pressed preceramic feedstock powder followed by electrical pyrolysis to obtain a bulk Zr-Si-O-C-B pellet.

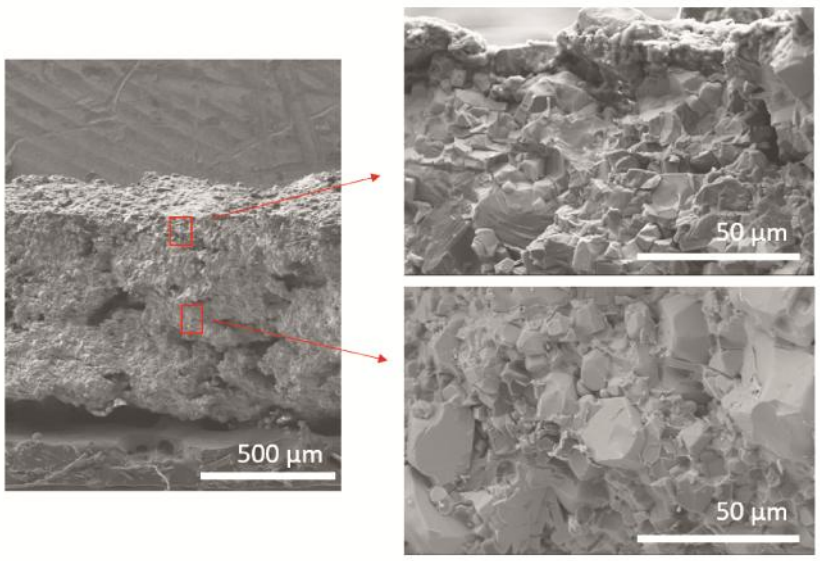

Figure S35. SEM observation of the cross-sectional view of a bulk Zr-Si-O-C-B pellet following electrical pyrolysis.

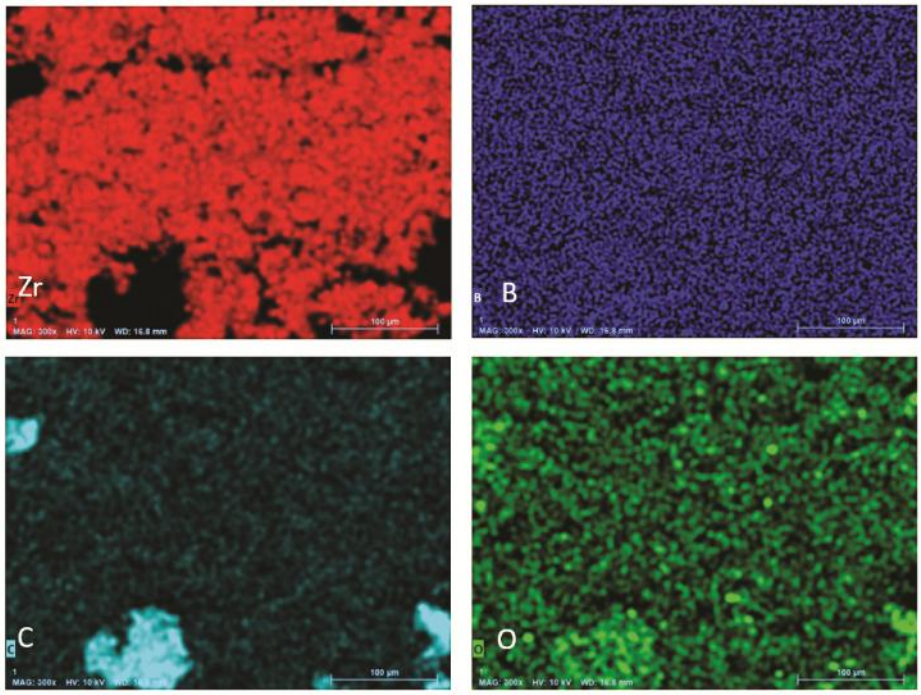

Figure S36. EDS mapping of the cross-sectional view of a bulk Zr-Si-O-C-B pellet following electrical pyrolysis.

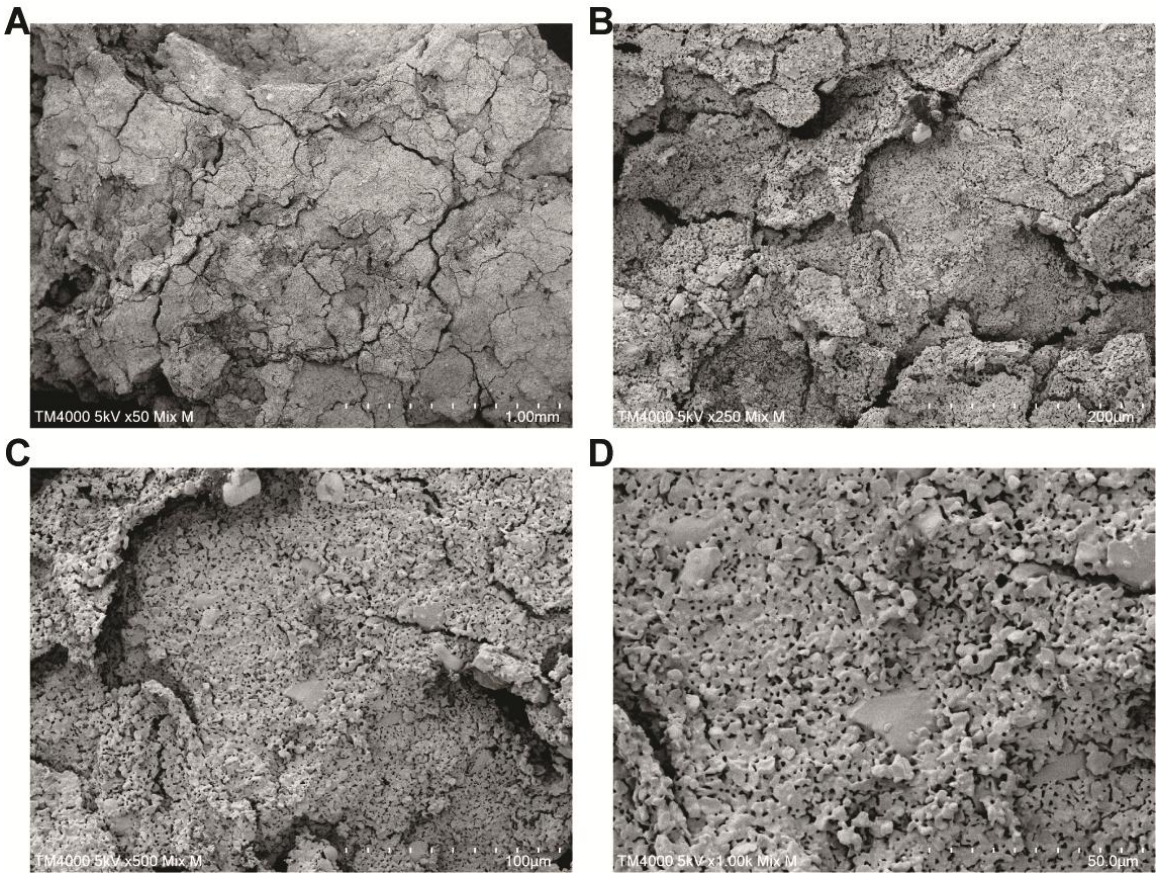

Figure S37. SEM observation of the plane view of bulk Cr-PCS with ZrB_2 filler particles as control.
(A) Under a magnification of 50x.
(B) Under a magnification of 250x.
(C) Under a magnification of 500x.
(D) Under a magnification of 1000x.

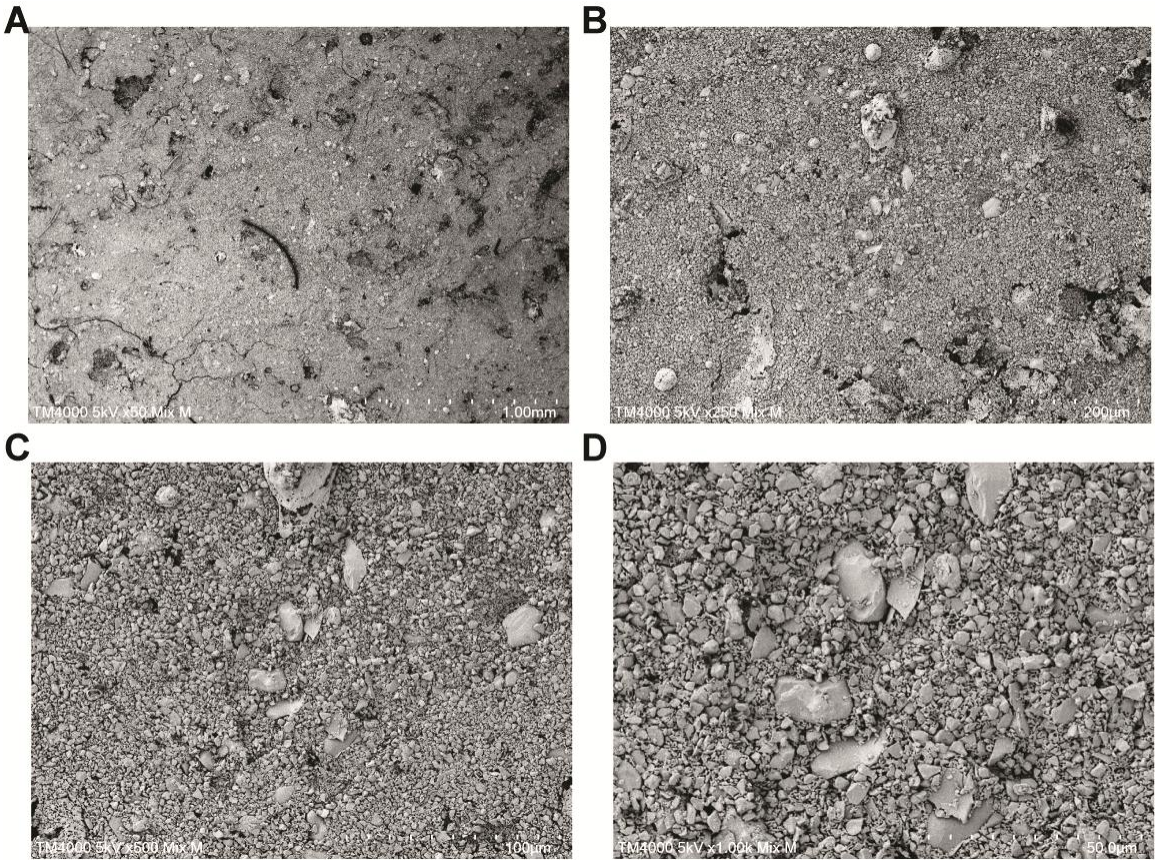

Figure S38. SEM observation of the plane view of bulk Cr-PCS with ZrB_2 filler particles and 2 wt.% Nb particles.

(A) Under a magnification of 50x.

(B) Under a magnification of 250x.

(C) Under a magnification of 500x.

(D) Under a magnification of 1000x.

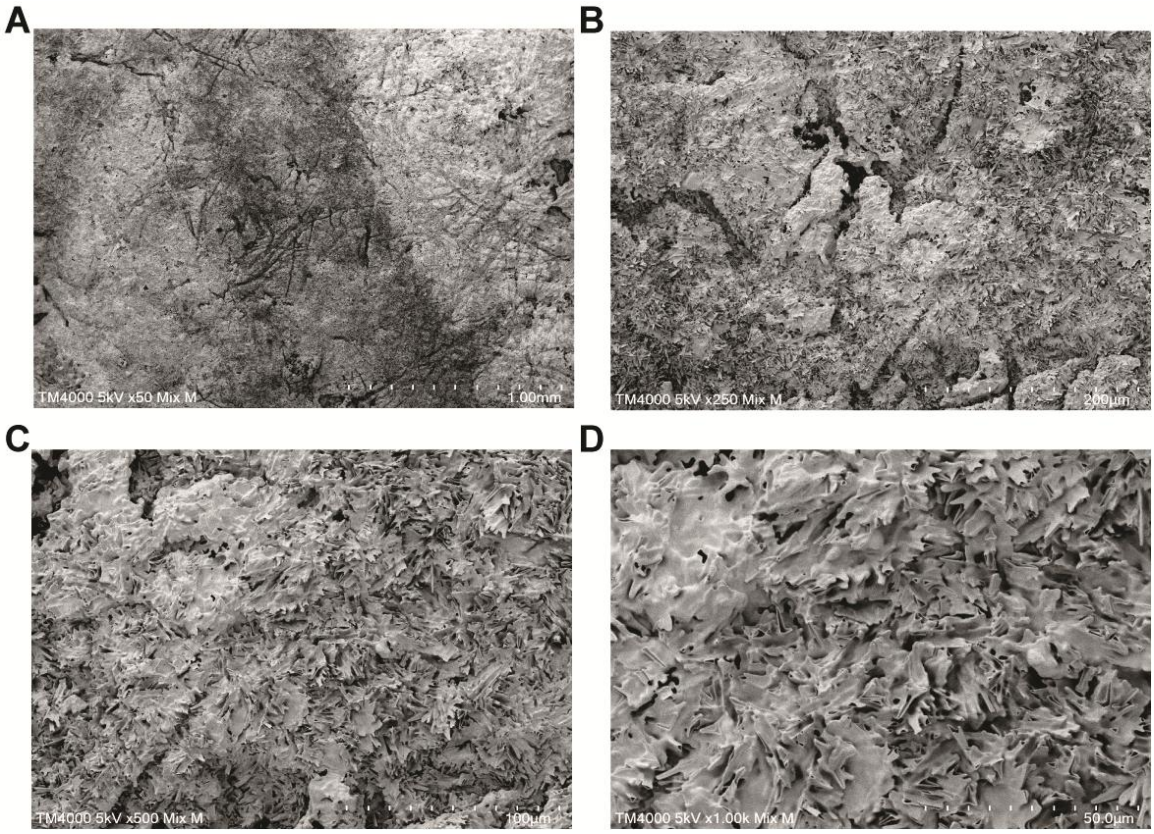

Figure S39. SEM observation of the plane view of bulk Cr-PCS with ZrB_2 filler particles and 4 wt.% Nb particles.

(A) Under a magnification of 50x.
(B) Under a magnification of 250x.
(C) Under a magnification of 500x.
(D) Under a magnification of 1000x.

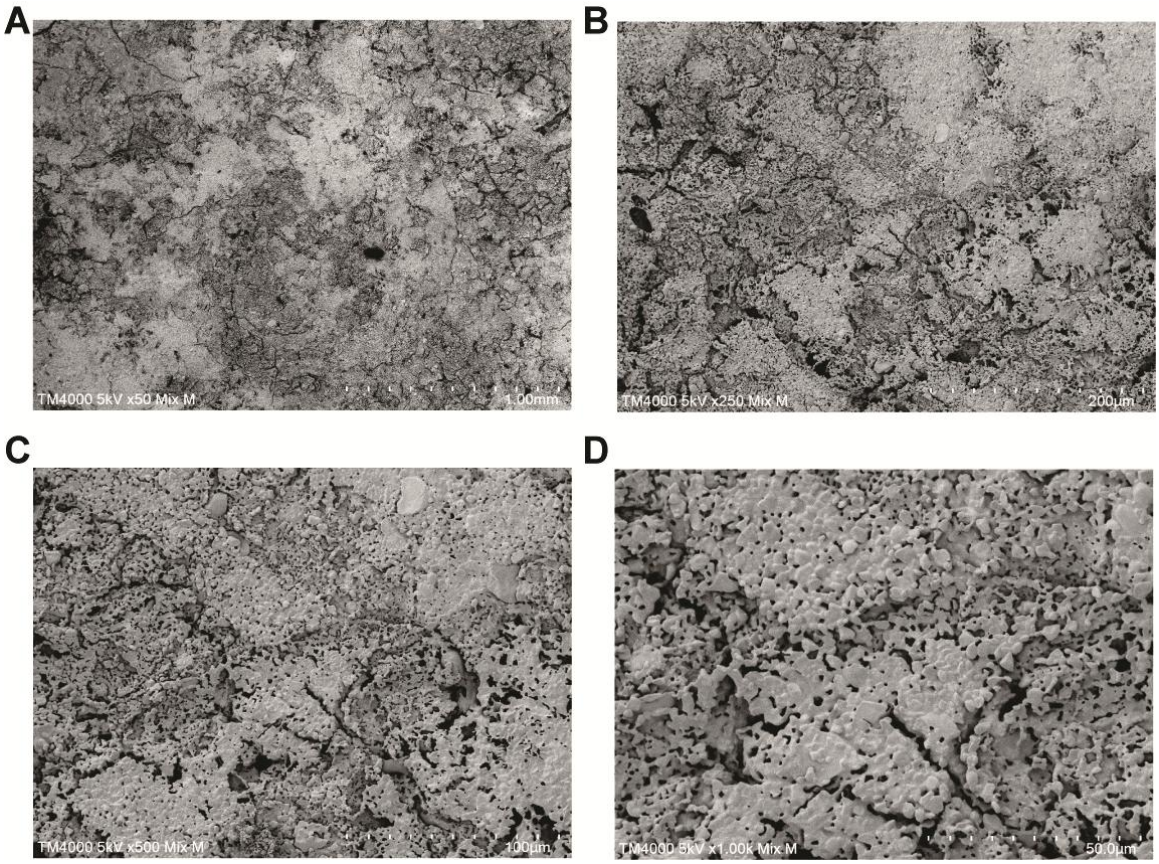

Figure S40. SEM observation of the plane view of bulk Cr-PCS with ZrB_2 filler particles and 6 wt.% Nb particles.

(A) Under a magnification of 50x.
(B) Under a magnification of 250x.
(C) Under a magnification of 500x.
(D) Under a magnification of 1000x.

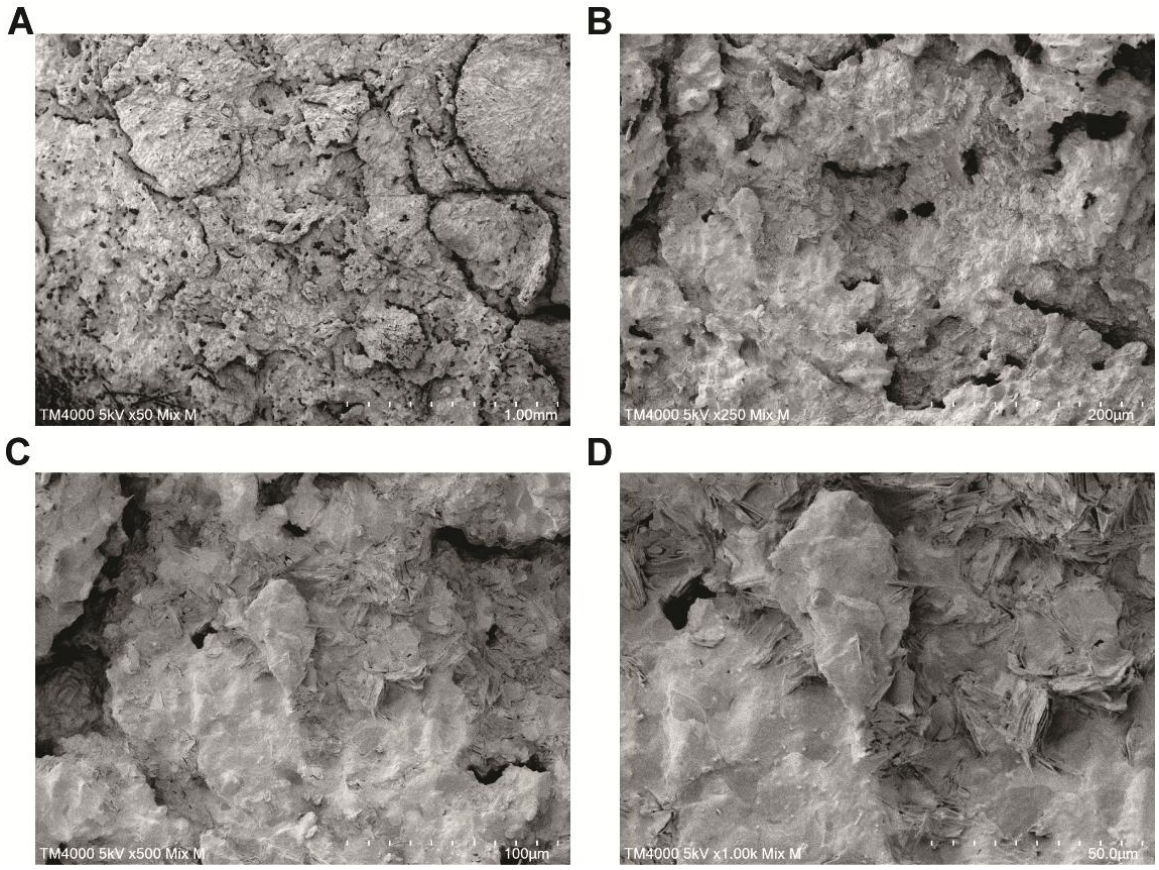

Figure S41. SEM observation of the plane view of bulk Cr-PCS with ZrB_2 filler particles and 8 wt.% Nb particles.

(A) Under a magnification of 50x.
(B) Under a magnification of 250x.
(C) Under a magnification of 500x.
(D) Under a magnification of 1000x.

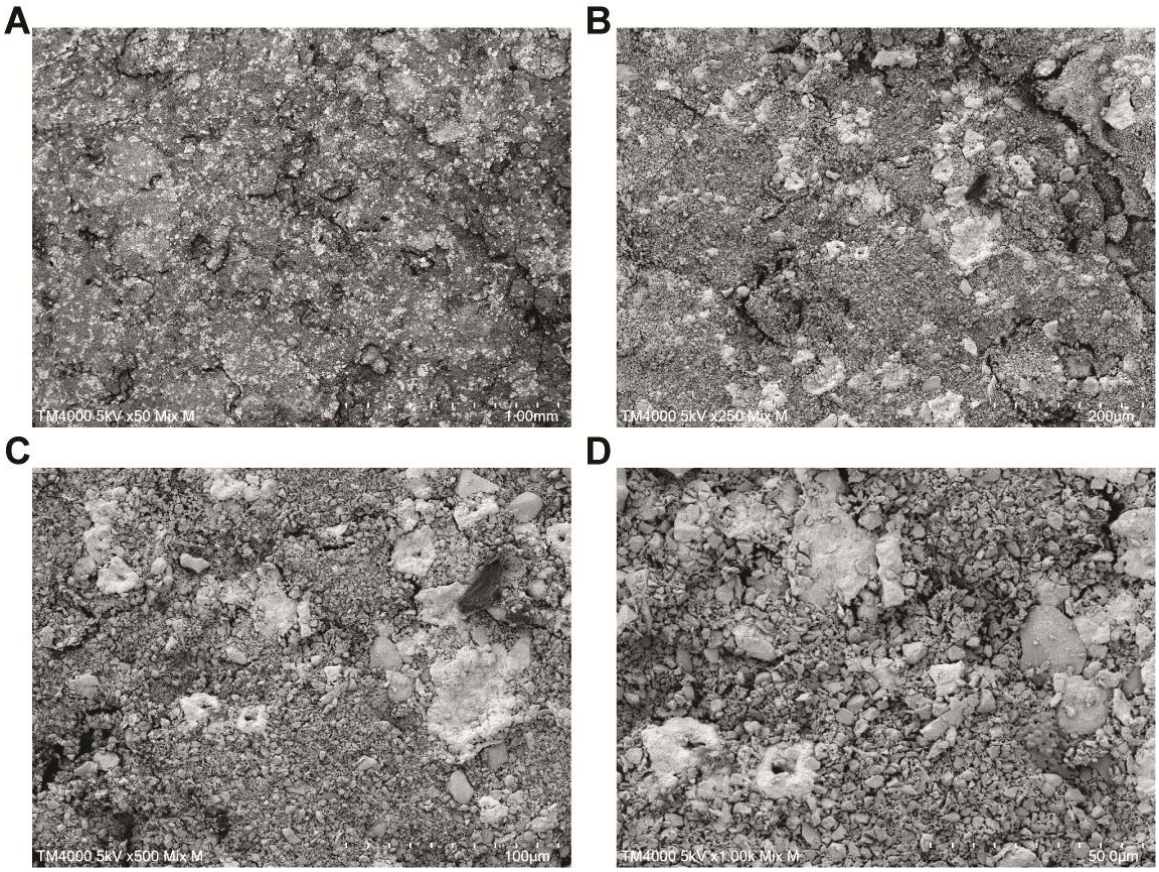

Figure S42. SEM observation of the plane view of bulk Cr-PCS with ZrB_2 filler particles and 10 wt.% Nb particles.

(A) Under a magnification of 50x.
(B) Under a magnification of 250x.
(C) Under a magnification of 500x.
(D) Under a magnification of 1000x.

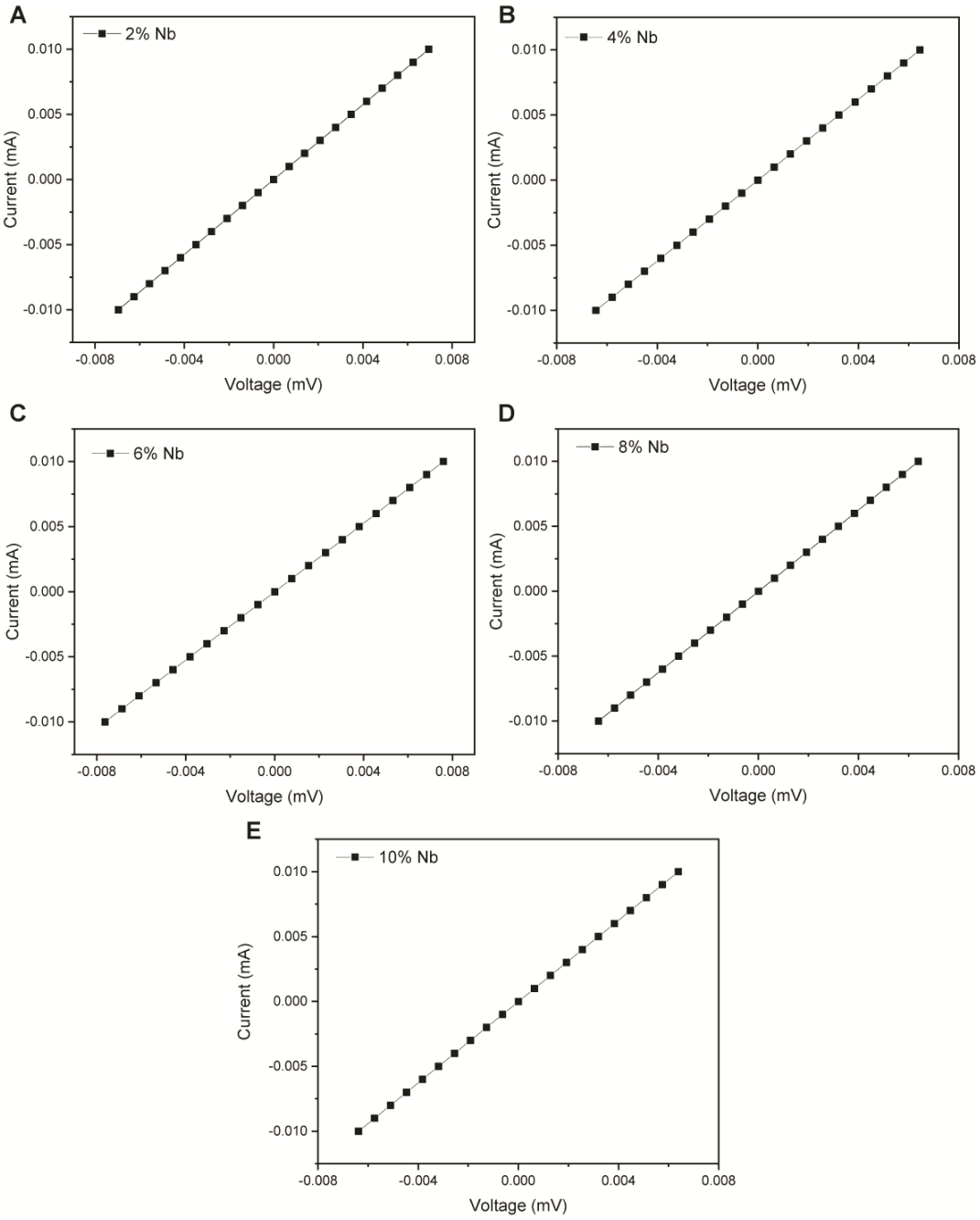

Figure S43. I-V characteristics of bulk Cr-PCS with ZrB_2 and Nb filler particles prepared using ultra high temperature sintering.

(A) Sample with 2 wt.% Nb.
(B) Sample with 4 wt.% Nb.
(C) Sample with 6 wt.% Nb.
(D) Sample with 8 wt.% Nb.
(E) Sample with 10 wt.% Nb.

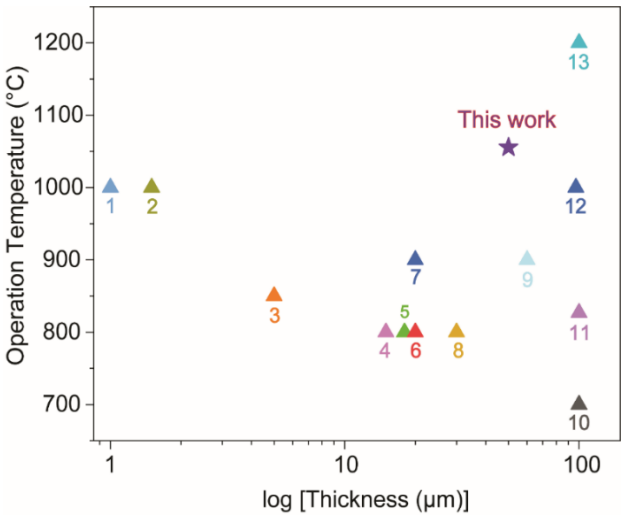

Figure S44. Ashby plot comparing thermal coating thickness vs. operating temperatures for coatings formed via PDC route; 1: SiCN (ABSE) + SiN (PHPS),[S1] 2: Polymethoxymethylsiloxane + hydroxy-terminated linear polysiloxane,[S2] 3: CrAlN + 2 mol.% YN,[S3] 4: Polyhydromethylsiloxane (or PHMS) + $TiSi_2$ (active filler) reinforced SiOC ceramic,[S4] 5: Poly(hydridomethylsiloxane) + $TiSi_2$ (expansion agent),[S5] 6: Poly(hydridomethylsiloxane) (PHMS) + Al/HW powders,[S6] 7: SiN,[S7] 8: $ZrSi_2$ as active filler + PHMS polymer as the precursor for the matrix,[S8] 9: (PHPS) + YSZ powder (passive filler) + barium powder,[S9] 10: Polyhydridomethylsiloxane (PHMS),[S10] 11: PSON (polysiloxane and polysilazane with a mass ratio of 5:2) + CeO_2 and B_4C as passive fillers,[S11] 12: SiOC/Al_2O_3/YSZ,[S12] 13: Yttrium di-silicate (Y-DS) and zircon coating on Si-SiC foams,[S13] and this work.

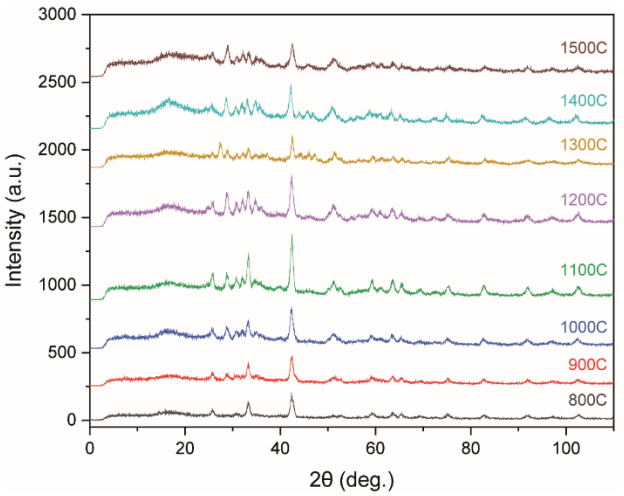

Figure S45. XRD plot depicting oxidation stability of ceramic samples at corresponding temperatures sintered in a tube furnace at 1000ºC.

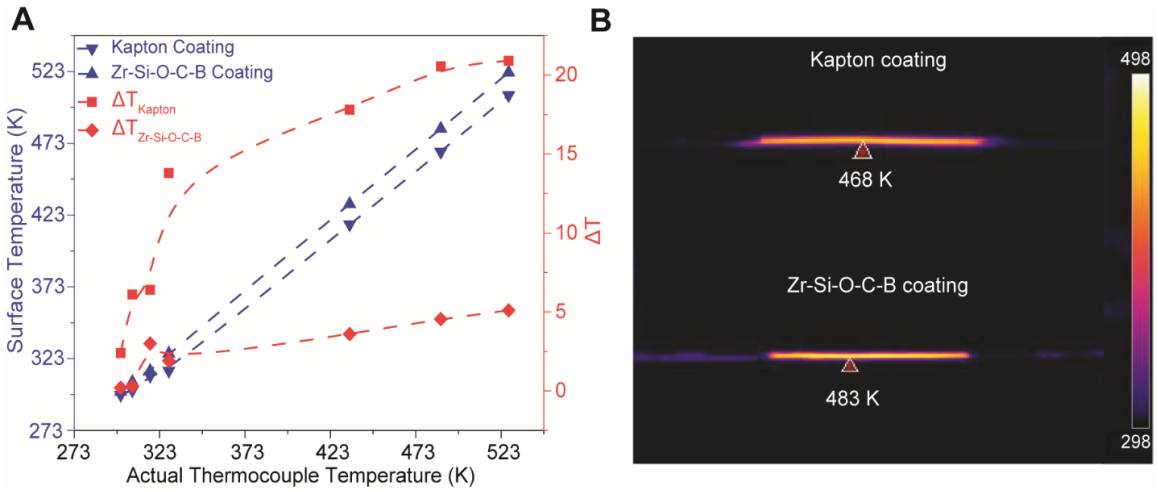

Figure S46. Emissivity studies.
(A) Plot depicting the emissive studies comparing Kapton®-coated and EPMC coated copper wires.
(B) An instance of the temperature difference between Kapton® - (top) and EPMC-coated (bottom) wires during heating with a surface temperature of 487.8 K.

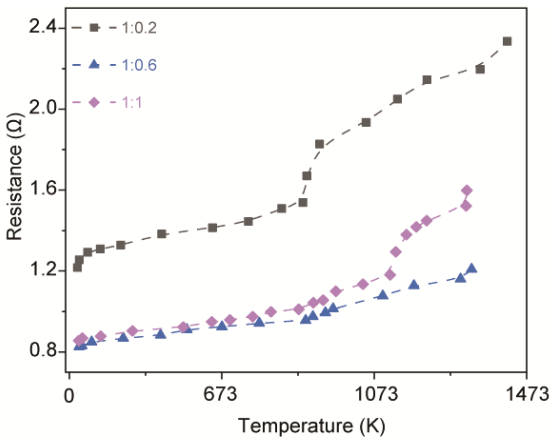

Figure S47. Plot depicting resistivity vs. temperature variation for different ratios of preceramic powders and solvents after ceramic conversion when subjected to oxygen-hydrogen torch test.

Figure S47 shows the evaluation of ceramic coatings for thermal management at elevated temperatures. The copper layer was coated with ceramic monolayer, which safeguards the metallic coating underneath against the thermal impact of the oxygen-hydrogen torch and protects against oxidation by restricting the diffusion of oxygen molecules inward and keeping the metal coating temperatures lower compared to their surroundings due to the high emissivity of the ceramic film. From the plot, all the ratios of ceramic powder to solvent are capable of withstanding elevated temperatures (> 1273 K), as the metal surface remains in pristine condition following the torch test and exhibits no signs of degradation or oxidation. Under these circumstances, the ceramic with 1:0.6 ratio displays the least change in resistivity, from 0.92 Ω.cm at 298.6 K to 1.35 Ω.cm at 1328.6 K (Supplementary Table S2 for torch test results for additional *M*-PCS coatings).

Table S2. Torch testing results for ceramics with different crosslinked metals.

Crosslinking element	$R_{initial}$	R_{final}
Hf	1.79 Ω (296.1 K)	6.37 kΩ (1258.1 K)
V	0.81 Ω (296.3 K)	1.55 kΩ (1337.1 K)
Cr	0.84 Ω (297.4 K)	1.40 Ω (1322.1 K)
Mo	0.92 Ω (295 K)	3.15 Ω (1313.1 K)
W	0.73 Ω (295.6 K)	0.77 Ω (1309.1 K)

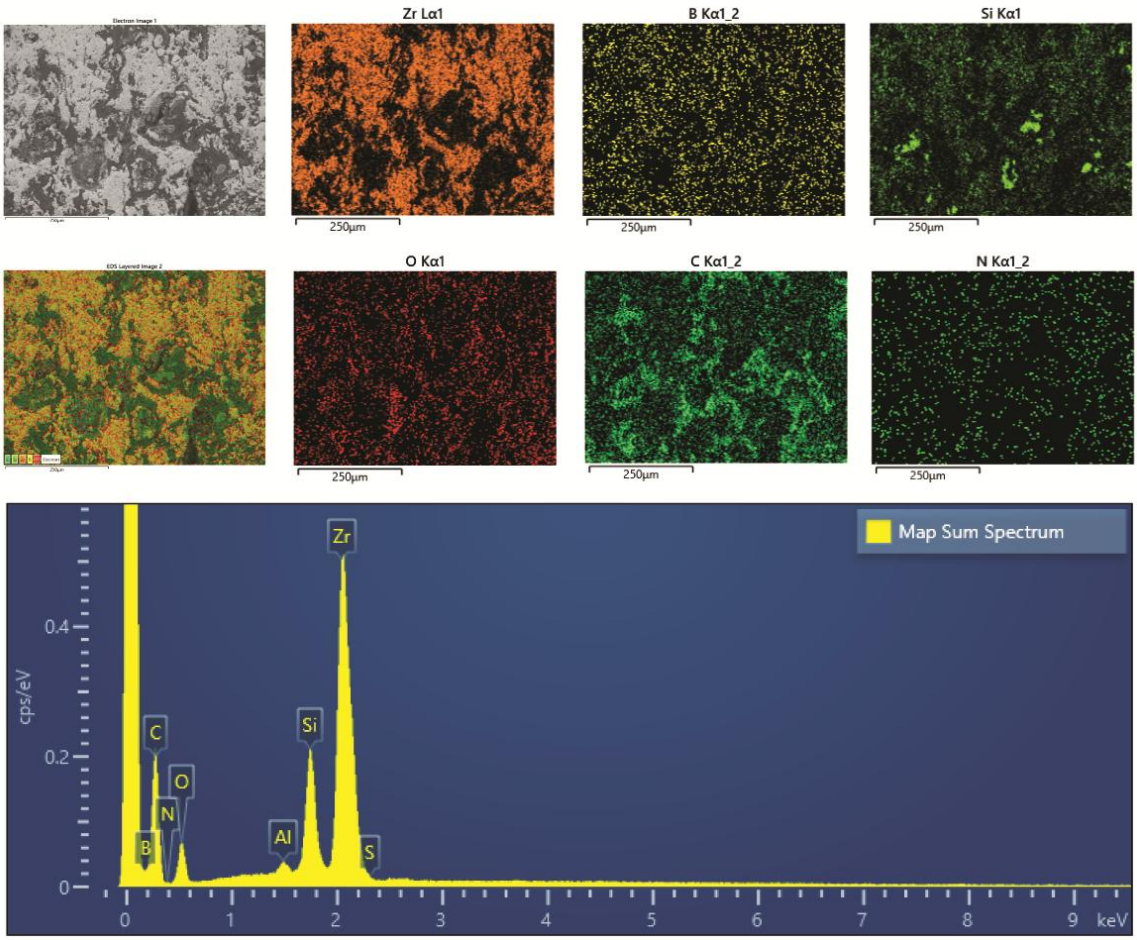

Figure 48. SEM and EDS mapping of the cross-section of bulk Zr-Si-O-C-B pellet following exposure at 1273 K under oxidative atmospheric conditions for a duration of one minute.

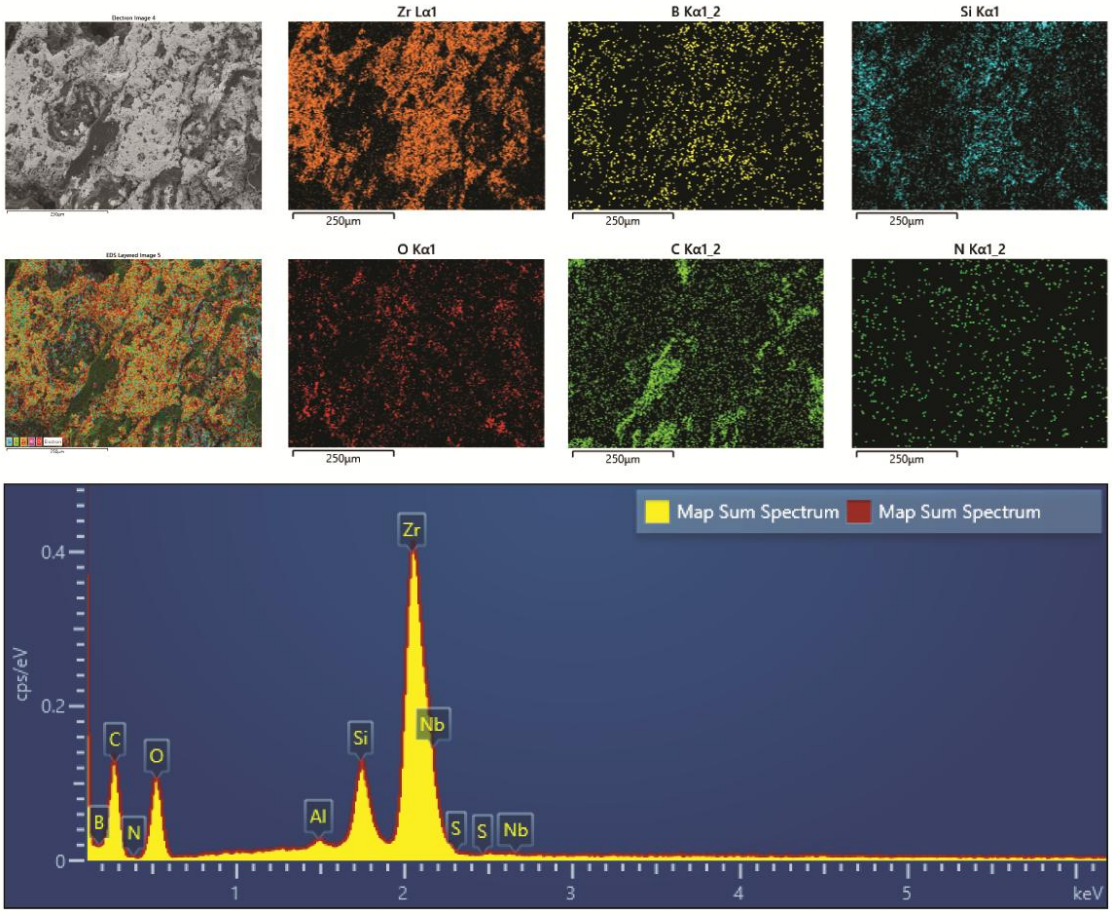

Figure S49. SEM and EDS mapping of the cross-section of bulk Zr-Si-O-C-B pellet following exposure at 1273 K under oxidative atmospheric conditions for a duration of 10 minutes.

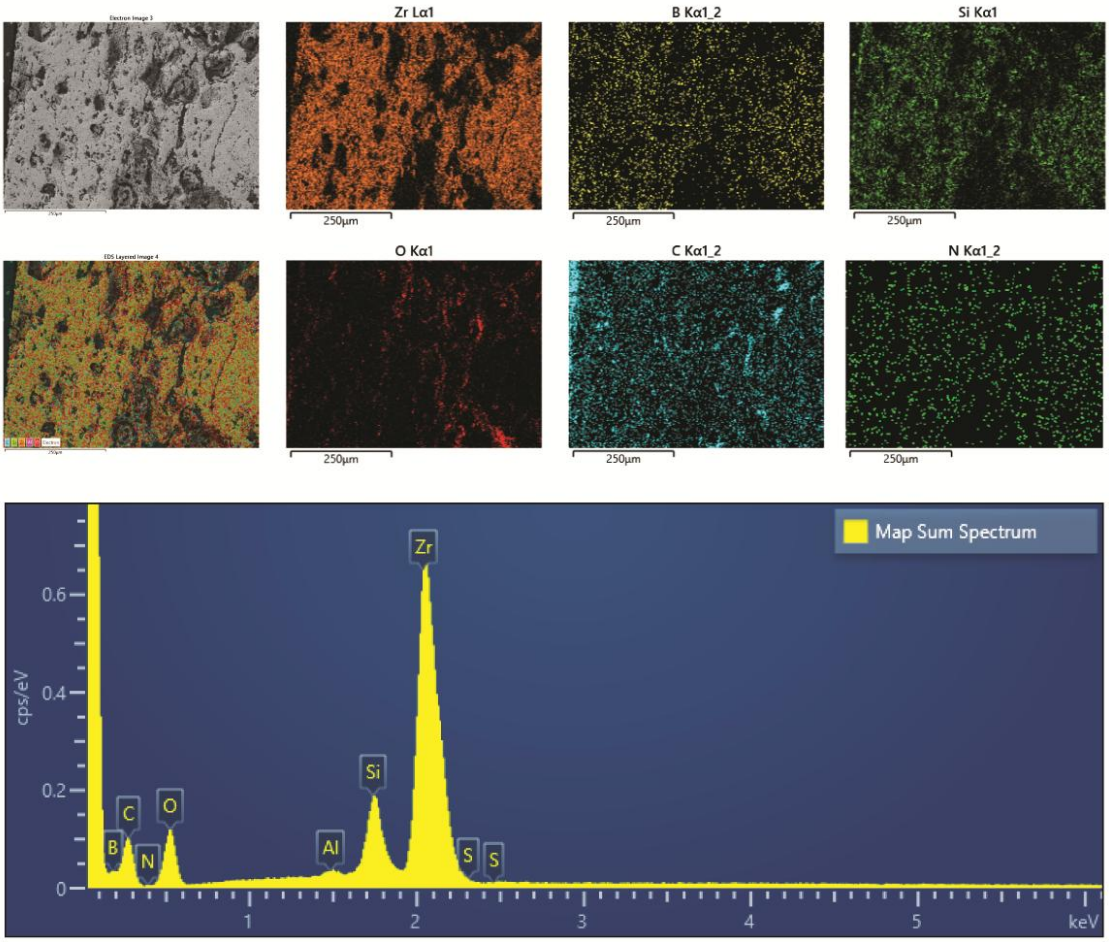

Figure S50. SEM and EDS mapping of the cross-section of bulk Zr-Si-O-C-B pellet following exposure at 1273 K under oxidative atmospheric conditions for a duration of 30 minutes.

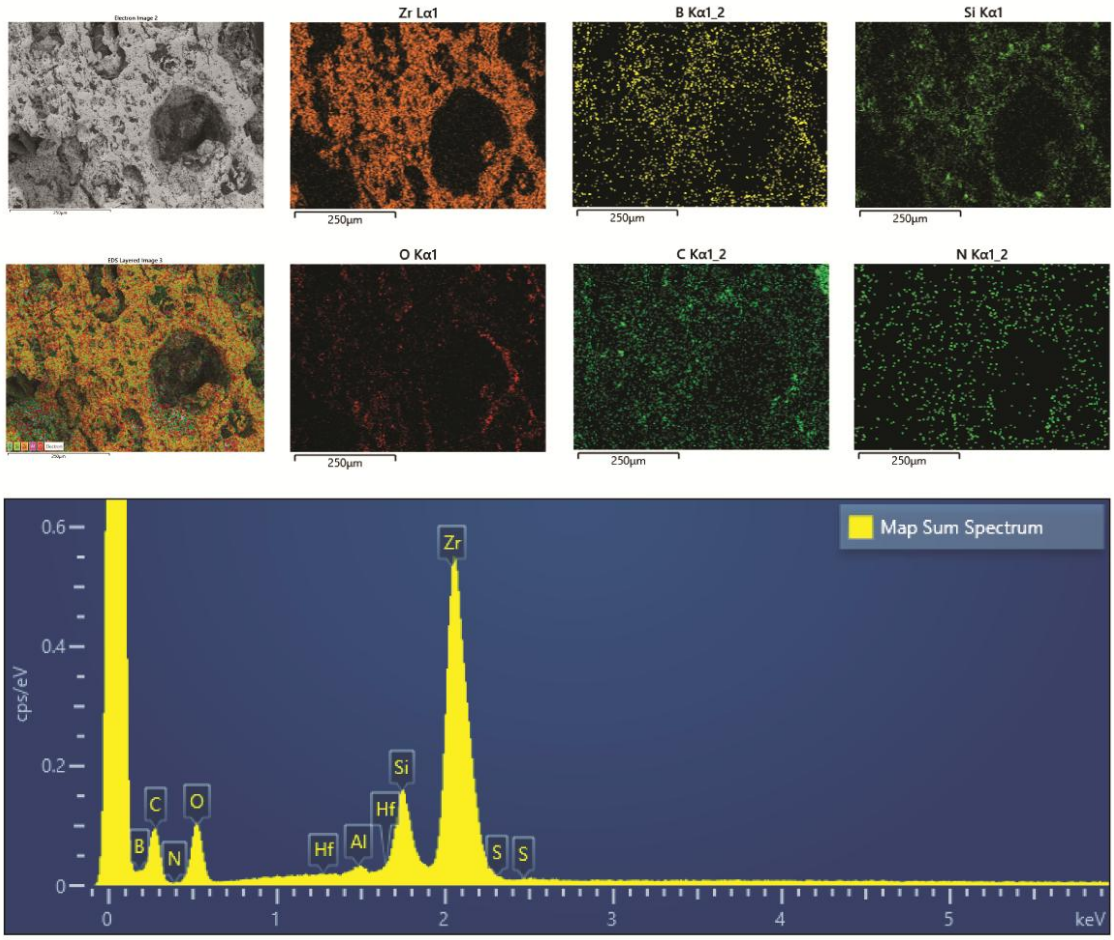

Figure S51. SEM and EDS mapping of the cross-section of bulk Zr-Si-O-C-B pellet following exposure at 1273 K under oxidative atmospheric conditions for a duration of 60 minutes.

Supplemental References

S1. Günthner, M., Kraus, T., Dierdorf, A., Decker, D., Krenkel, W., and Motz, G. (2009). Advanced coatings on the basis of Si (C) N precursors for protection of steel against oxidation. Journal of the European Ceramic Society *29*, 2061-2068.

S2. Kappa, M., Kebianyor, A., and Scheffler, M. (2010). A two-component preceramic polymer system for structured coatings on metals. Thin Solid Films *519*, 301-305.

S3. Braun, R., Rovere, F., Mayrhofer, P.H., and Leyens, C. (2010). Environmental protection of γ-TiAl based alloy Ti-45Al-8Nb by CrAlYN thin films and thermal barrier coatings. Intermetallics *18*, 479-486.

S4. Wang, K., Unger, J., Torrey, J.D., Flinn, B.D., and Bordia, R.K. (2014). Corrosion resistant polymer derived ceramic composite environmental barrier coatings. Journal of the European Ceramic Society *34*, 3597-3606.

S5. Torrey, J.D., and Bordia, R.K. (2008). Processing of polymer-derived ceramic composite coatings on steel. Journal of the American Ceramic Society *91*, 41-45.

S6. Wang, Y., Tian, H., Quan, D., Guo, L., Ouyang, J., Zhou, Y., and Jia, D. (2012). Preparation, characterization and infrared emissivity properties of polymer derived coating formed on 304 steel. Surface and Coatings Technology *206*, 3772-3776.

S7. Riffard, F., Joannet, E., Buscail, H., Rolland, R., and Perrier, S. (2017). Beneficial effect of a pre-ceramic polymer coating on the protection at 900° C of a commercial AISI 304 stainless steel. Oxidation of Metals *88*, 211-220.

S8. Wang, K., Günthner, M., Motz, G., and Bordia, R.K. (2011). High performance environmental barrier coatings, Part II: Active filler loaded SiOC system for superalloys. Journal of the European Ceramic Society *31*, 3011-3020.

S9. Parchovianská, I., Parchovianský, M., Medveď, D., and Galusek, D. (2023). Thermal shock behavior and high-temperature oxidation performance of PDC-based environmental barrier coatings on AISI 441 stainless steel. Surface and Coatings Technology *474*, 130074.

S10. Blum, Y.D., Hui, D.K., and MacQueen, D.B. (2012). Method of imparting corrosion resistance to a substrate surface, and coated substrates prepared thereby. Google Patents.

S11. Li, J., and Luo, Z. (2020). Fabrication and performances of preceramic polymer-based high-temperature High emissivity coating. Journal of the European Ceramic Society *40*, 5217-5225.

S12. Tian, Z., Zhu, W., Yan, X., and Su, D. (2022). Passive Filler-Loaded Silicon Oxycarbide Coating on Nickle Alloy with High Thermal Shocking Behavior and Oxidation Resistance. Materials *15*, 6395.

S13. Bernardo, E., Fiocco, L., Parcianello, G., Storti, E., and Colombo, P. (2014). Advanced ceramics from preceramic polymers modified at the nano-scale: A review. Materials *7*, 1927-1956.